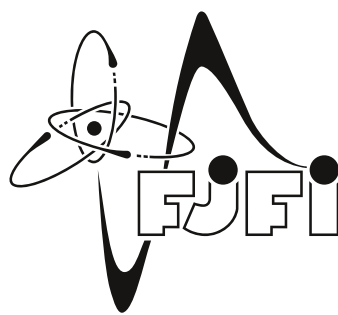


Czech Technical University in Prague  
Faculty of Nuclear Sciences and Physical Engineering

Department of Physics  
Nuclear and Particle Physics



# Coherent photoproduction of $\rho$ in oxygen–oxygen collisions

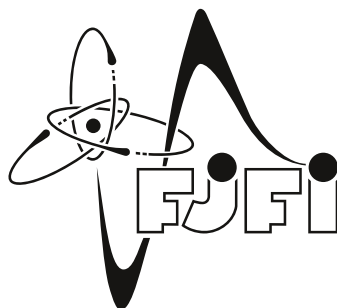
Bachelor's thesis

Author: Jakub Juračka  
Supervisor: prof. Jesús Guillermo Contreras Nuño, Ph.D.  
Consultant: Ing. Tomáš Herman  
Year: 2023



České vysoké učení technické v Praze  
Fakulta jaderná a fyzikálně inženýrská

Katedra fyziky  
Jaderná a částicová fyzika



# Koherentní fotoprodukce $\rho$ v kyslík-kyslíkových srážkách

Bakalářská práce

Autor: Jakub Juračka  
Vedoucí práce: prof. Jesús Guillermo Contreras Nuño, Ph.D.  
Konzultant: Ing. Tomáš Herman  
Rok: 2023



# ZADÁNÍ BAKALÁŘSKÉ PRÁCE

Akademický rok: 2022/2023



*Student:* Jakub Juračka

*Studijní program:* Jaderná a částicová fyzika

*Název práce:* Koherentní fotoprodukce  $\rho$  v kyslík-kyslíkových srážkách  
(česky)

*Název práce:* Coherent photoproduction of  $\rho$  in oxygen-oxygen collisions  
(anglicky)

*Jazyk práce:* Angličtina

*Pokyny pro vypracování:*

1) Vypracování rešerše na téma:

- a) Měření koherentní fotoprodukce  $\rho$  na ALICE
- b) STARlight model pro koherentní fotoprodukcí  $\rho$

2) Analýza koherentní fotoprodukce  $\rho$  v kyslík-kyslíkových srážkách na ALICE s použitím STARlight

*Doporučená literatura:*

- [1] ALICE Collaboration. (2020). Coherent photoproduction of rho(0) vector mesons in ultra-peripheral Pb-Pb collisions at s(NN)= 5.02 TeV. The Journal, 6.
- [2] ALICE Collaboration. (2021). First measurement of coherent rho(0) photoproduction in ultra-peripheral Xe-Xe collisions at s(NN) = 5.44 TeV. Physics Letters B, 820.
- [3] Klein, S. R., and Nystrand, J. (1999). Exclusive vector meson production in relativistic heavy ion collisions. Physical Review C, 60(1).
- [4] Klein, S. R., Nystrand, J., Seger, J., Gorbunov, Y., and Butterworth, J. (2017). STARlight: A Monte Carlo simulation program for ultra-peripheral collisions of relativistic ions. Computer Physics Communications, 212, 258-268.

*Jméno a pracoviště vedoucího bakalářské práce:*

prof. Jesús Guillermo Contreras Nuño, Ph.D.  
Katedra fyziky, Fakulta jaderná a fyzikálně inženýrská ČVUT v Praze

*Jméno a pracoviště konzultanta:*

Ing. Tomáš Herman  
Katedra fyziky, Fakulta jaderná a fyzikálně inženýrská ČVUT v Praze

*Datum zadání bakalářské práce:* 20.10.2022

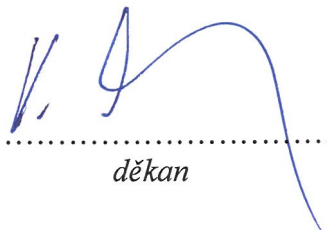
*Termín odevzdání bakalářské práce:* 02.08.2023

*Doba platnosti zadání je dva roky od data zadání.*

  
.....  
garant studijního programu



  
.....  
vedoucí katedry

  
.....  
děkan

*V Praze dne* 20.10.2022



## PROHLÁŠENÍ

Já, níže podepsaný

*Jméno a příjmení studenta:* Jakub Juračka  
*Osobní číslo:* 502392  
*Název studijního programu (oboru):* Jaderná a částicová fyzika

prohlašuji, že jsem bakalářskou práci s názvem:

**Koherentní fotoprodukce ró v kyslík-kyslíkových srážkách**

vypracoval samostatně a uvedl veškeré použité informační zdroje v souladu s Metodickým pokynem o dodržování etických principů při přípravě vysokoškolských závěrečných prací.

V Praze dne 7. 7. 2023

.....  
  
podpis

## **Acknowledgements**

I would like to express my sincere gratitude to my supervisor, Jesús Guillermo Contreras Nuño, for his expert guidance along my first steps into a scientific career, his patience with my many questions, invaluable advice, and profound insight into any topic which may have piqued my interest. Many thanks also belong to my consultant, Tomáš Herman, for his dedication and constant willingness to help and offer swathes of his personal time whenever I required it. Furthermore, I would like to acknowledge the aid of Diana Krupová in matters concerning the  $O^2$  analysis framework, without which my work would not have progressed far. And lastly, I must emphasise the scarcely expressed appreciation for my friends and family for their unconditional support in my endeavours.



*Title:*

**Coherent photoproduction of  $\rho$  in oxygen–oxygen collisions**

*Author:* Jakub Juračka

*Study programme:* Nuclear and Particle Physics

*Work:* Bachelor’s thesis

*Supervisor:* prof. Jesús Guillermo Contreras Nuño, Ph.D.  
Department of Physics, Faculty of Nuclear Sciences and Physical Engineering, Czech Technical University in Prague

*Consultant:* Ing. Tomáš Herman  
Department of Physics, Faculty of Nuclear Sciences and Physical Engineering, Czech Technical University in Prague

*Abstract:* Coherent photoproduction of vector mesons occurring in ultra-peripheral collisions (UPCs) is an extensively studied process, as it enables the examination of the inner structure of nuclei—namely their gluon distributions. This may provide new insight into the quantitative behaviour of important QCD phenomena, such as gluon saturation or nuclear shadowing. In this work, UPCs and the photoproduction process are described in more detail. Two previous measurements of  $\rho$  photoproduction performed by the ALICE Collaboration on data from Pb–Pb and Xe–Xe collisions are examined. Subsequently, preliminary analysis of a dataset of O–O (and Pb–Pb) collisions simulated with the STARlight program is performed, focusing on the calculation of  $A \times E$  correction factors.

*Keywords:* ALICE, STARlight, O–O collisions,  $\rho$  photoproduction,  $A \times E$

*Název práce:*

**Koherentní fotoprodukce  $\rho$  v kyslík-kyslíkových srážkách**

*Autor:* Jakub Juračka

*Studijní program:* Jaderná a částicová fyzika

*Druh práce:* Bakalářská práce

*Vedoucí práce:* prof. Jesús Guillermo Contreras Nuño, Ph.D.  
Katedra fyziky, Fakulta jaderná a fyzikálně inženýrská, České vysoké učení technické v Praze

*Konzultant:* Ing. Tomáš Herman  
Katedra fyziky, Fakulta jaderná a fyzikálně inženýrská, České vysoké učení technické v Praze

*Abstrakt:* Koherentní fotoprodukce vektorových mezonů nastávající v ultra-periferních srážkách (UPCs) je často studovaným procesem, jelikož umožňuje zkoumat vnitřní strukturu jader – konkrétně jejich gluonové distribuce. Toto může dovolit blíže zkoumat chování důležitých jevů v QCD, jako je gluonová saturace nebo jaderné stínění. V této práci jsou UPCs a proces fotoprodukce popsány podrobněji. Jsou zkoumána dvě předchozí měření fotoprodukce  $\rho$  provedená kolaborací ALICE na datech z Pb–Pb a Xe–Xe srážek. Následně je provedena předběžná analýza souboru dat z O–O (a Pb–Pb) srážek simulovaných programem STARlight se zaměřením na výpočet  $A \times E$  korekčních faktorů.

*Klíčová slova:* ALICE, STARlight, O–O srážky, fotoprodukce  $\rho$ ,  $A \times E$

# Contents

List of figures	xiii
List of tables	xv
Preface	1
<b>1 Introduction to particle physics</b>	<b>2</b>
1.1 Fundamental quantities and variables	2
1.1.1 Energy, mass, and momentum	2
1.1.2 Rapidity and pseudorapidity	2
1.1.3 Cross section and luminosity	3
1.2 Standard Model	3
1.2.1 Forces	3
1.2.2 Particles	5
<b>2 Basics of QCD</b>	<b>8</b>
2.1 Colour	8
2.2 QCD coupling constant	9
2.3 Deep-inelastic scattering experiments	9
2.3.1 Saturation	10
2.3.2 Nuclear shadowing	11
<b>3 Ultra-peripheral collisions and photoproduction</b>	<b>12</b>
3.1 Photon flux	12
3.2 Exclusive vector meson photoproduction	14
3.2.1 STARlight model for coherent photoproduction of $\rho$	15
<b>4 CERN, the LHC, and ALICE</b>	<b>18</b>
4.1 CERN	18
4.2 LHC	18
4.2.1 Design and operation	19
4.2.2 LHC collision systems	20
4.3 ALICE	22
4.3.1 Detectors	23
4.3.2 Continuous readout mode and the $O^2$ analysis framework	26
<b>5 Previous ALICE measurements of coherent photoproduction of <math>\rho^0</math></b>	<b>30</b>
5.1 $\rho^0$ photoproduction in Pb–Pb UPCs at $\sqrt{s_{NN}} = 5.02$ TeV	30
5.1.1 Experimental set-up	30
5.1.2 Analysis procedure	31
5.1.3 Results	33

5.2	$\rho^0$ photoproduction in Xe–Xe UPCs at $\sqrt{s_{\text{NN}}} = 5.44$ TeV . . . . .	35
5.2.1	Experimental set-up . . . . .	35
5.2.2	Analysis procedure . . . . .	35
5.2.3	Results . . . . .	37
<b>6</b>	<b>Analysis of simulated data</b>	<b>39</b>
6.1	STARlight MC generator . . . . .	39
6.2	O–O dataset . . . . .	40
6.2.1	Generator-level data . . . . .	40
6.2.2	Reconstructed data selection . . . . .	41
6.2.3	A×E calculation . . . . .	44
6.3	Pb–Pb dataset . . . . .	47
6.3.1	Generator-level data . . . . .	47
6.3.2	Reconstructed data selection . . . . .	48
6.3.3	A×E calculation . . . . .	48
6.4	Analysis results summary . . . . .	48
	<b>Summary</b>	<b>54</b>
	<b>A STARlight setup parameters</b>	<b>I</b>
	<b>Bibliography</b>	<b>II</b>

# List of figures

1.1	Standard Model classification of elementary particles. . . . .	5
2.1	Diagram of quark interactions via a gluon exchange. . . . .	8
2.2	Parton distribution functions of proton constituents. . . . .	10
2.3	Nuclear effects on PDFs and shadowing $A$ -dependence. . . . .	11
3.1	Schematic of an ultra-peripheral collision between two nuclei. . . . .	13
3.2	Schematic of $\rho^0$ photoproduction in a heavy-ion UPC. . . . .	15
3.3	Plot of $d\sigma/dt$ for coherent $\rho$ production. . . . .	17
3.4	Photon energy dependence of photonuclear cross sections of coherent production of vector mesons. . . . .	17
4.1	Diagram of the CERN accelerator complex as of 2022. . . . .	19
4.2	Projection of LHC long-term operation schedule as of January 2022. . . . .	20
4.3	Simulated performance of an O–O run. . . . .	22
4.4	Diagram of the ALICE detector. . . . .	23
4.5	Layout of the FIT subdetectors. . . . .	26
4.6	Diagram of the innermost central barrel detectors of ALICE. . . . .	27
4.7	Data processing flow of the O <sup>2</sup> system. . . . .	29
5.1	Invariant mass and transverse momentum distributions for track pairs passing the selection criteria for Pb–Pb UPCs. . . . .	31
5.2	$A \times E$ corrections for photoproduction in Pb–Pb UPCs. . . . .	32
5.3	Fitted invariant mass distribution of the $\rho^0$ mesons photoproduced in Pb–Pb UPCs. . . . .	33
5.4	Cross sections of coherent photoproduction of $\rho^0$ mesons in Pb–Pb UPCs. . . . .	34
5.5	Invariant mass and transverse momentum distributions for track pairs passing the selection criteria for Xe–Xe UPCs. . . . .	36
5.6	$A \times E$ corrections for photoproduction in Xe–Xe UPCs. . . . .	36

5.7	Fitted invariant mass distribution of selected pion pairs in Xe–Xe UPCs. . .	37
5.8	Cross section of coherent photoproduction of $\rho^0$ mesons in Xe–Xe UPCs. . .	38
5.9	$A$ -dependence of $\sigma_{\gamma A}$ for coherent $\rho^0$ production. . . . .	38
6.1	Generator-level invariant mass, transverse momentum, and rapidity distributions of generated $\rho^0$ mesons from O–O events. . . . .	42
6.2	Transverse momentum, azimuthal angle, and rapidity distributions of generated pion tracks from O–O events. . . . .	43
6.3	Select track selection properties of O–O data reconstructed tracks passing the PID requirement. . . . .	44
6.4	$A \times E$ corrections for $\rho^0$ invariant mass distribution reconstructed from O–O data. . . . .	46
6.5	$A \times E$ corrections for $\rho^0$ transverse momentum distribution reconstructed from O–O data. . . . .	46
6.6	$A \times E$ corrections for $\rho^0$ rapidity distribution reconstructed from O–O data. . . . .	47
6.7	Generator-level invariant mass, transverse momentum, and rapidity distributions of generated $\rho^0$ mesons from Pb–Pb events. . . . .	49
6.8	Transverse momentum, azimuthal angle, and rapidity distributions of generated pion tracks from Pb–Pb events. . . . .	50
6.9	Select track selection properties of Pb–Pb data reconstructed tracks passing the PID requirement. . . . .	51
6.10	$A \times E$ corrections for $\rho^0$ invariant mass distribution reconstructed from Pb–Pb data. . . . .	51
6.11	$A \times E$ corrections for $\rho^0$ transverse momentum distribution reconstructed from Pb–Pb data. . . . .	52
6.12	$A \times E$ corrections for $\rho^0$ rapidity distribution reconstructed from Pb–Pb data. . . . .	52

# List of tables

3.1	Lorentz boost factors for particle beams accelerated in the LHC. . . . .	14
4.1	Collision systems and their $\sqrt{s_{NN}}$ studied by the LHC experiments in Runs 1 and 2. . . . .	20
6.1	Constant function fit results for A×E values calculated for $m$ , $p_T$ , and $y$ spectra obtained from the O–O data. . . . .	45
6.2	Constant function fit results for A×E values calculated for $m$ , $p_T$ , and $y$ spectra obtained from the Pb–Pb data. . . . .	48
A.1	Full list of utilised STARlight setup parameters. . . . .	I

# Preface

One of the first things a student is taught in their lessons of physics is that the term 'atom' comes from the ancient Greek word for *indivisible*. The idea of something elementary forming all matter around us has been puzzling scientists and philosophers for millennia. The notion of the exact nature of this substratum kept changing as our knowledge improved, but it was not until the last century that we finally began to peer into the subatomic world. Just as microscopes greatly surpassed the capabilities of the human eye, high energy physics (HEP) experiments unlocked yet another, previously unreachable, scale. Deep-inelastic scattering and ultra-peripheral collision studies are at the cutting edge of active research into the structure of nucleons, trying to answer questions which have so far gone unanswered.

Chapter 1 of this thesis introduces select elementary variables and physical quantities used in particle physics and presents an overview of the Standard Model and its description of elementary particles and the fundamental interactions.

Chapter 2 develops several of the aforementioned concepts further using the framework of QCD, the theory behind the strong interaction. Certain practical aspects and experimental facts of QCD processes are introduced, including nuclear shadowing and gluon saturation, both of relevance for this work as the main motivation behind the study of UPCs and photoproduction. These are covered in more detail in Chapter 3, alongside the various models used for the description of the photoproduction process.

CERN, the LHC, and the ALICE detector are explored in Chapter 4. Information concerning the collision systems is summarised, with special importance given to the proposed O–O run. Also present is the synopsis of the upgrades to the ALICE detector in preparation for the LHC restart after Long Shutdown 2 and the switch to a new data collection scheme and computing framework.

Previous measurements of  $\rho^0$  photoproduction from the ALICE Collaboration are reported in Chapter 5.

Finally, Chapter 6 outlines a preliminary analysis performed on a dataset of  $\rho^0$  photoproduction in O–O (and Pb–Pb) UPCs generated using the STARlight MC generator. Its primary focus was the calculation of acceptance times efficiency ( $A \times E$ ) correction factors.



# Chapter 1

## Introduction to particle physics

Given both the specific area of study and experimental methods of particle physics, it operates with a unique set of physical quantities, units, and theoretical concepts, the majority of which are rarely used outside this field. Several of these will be introduced in this chapter. It should be noted that this is not intended as an exhaustive and comprehensive list, but rather a collection of elementary definitions and information about the subject matter further expanded upon in the remainder of the thesis.

### 1.1 Fundamental quantities and variables

#### 1.1.1 Energy, mass, and momentum

Although not unique to the field of HEP, these three observables represent some of the most important and widely used descriptors of the properties of particles. Energy ( $E$ ) and momentum ( $\vec{p}$ ) are often linked in the four-momentum four-vector  $P = (E/c, \vec{p})$  (with  $c$  being the speed of light in vacuum), whose square defines the particle's invariant mass ( $m$ ). This is frequently written in the form of the energy-momentum relation,

$$E^2 = p^2 c^2 + m^2 c^4, \quad (1.1)$$

which is an essential equation for particle physics.

When describing events in particle colliders, it is customary to align one of the axes of the chosen reference frame with the direction of the particle beam and divide the momentum vector into two parts. The vector component along this axis is then called longitudinal momentum (denoted  $p_L$ ), which generally changes when Lorentz transformations are performed (i.e. it is not invariant). However, the vector components along the two perpendicular axes are Lorentz invariant and are usually grouped into the transverse momentum ( $\vec{p}_T$ ) vector.

#### 1.1.2 Rapidity and pseudorapidity

The longitudinal momentum of a particle together with its energy can be used to define its rapidity, another important parameter for accelerator physics. In special relativity, rapidity has certain geometrical implications, but for the description of particles in high

energy physics it is defined as

$$y = \frac{1}{2} \ln \left( \frac{E + p_L c}{E - p_L c} \right). \quad (1.2)$$

It may be thought of as the relativistic equivalent of speed. While rapidity itself is not a Lorentz-invariant variable, the difference of rapidities is invariant with respect to Lorentz boosts along the beam axis.

Pseudorapidity may be defined as

$$\eta = -\ln \left( \tan \frac{\theta}{2} \right). \quad (1.3)$$

It requires the measurement of only one variable ( $\theta$ , the angle between the momentum of the particle and the beam axis). At sufficiently high energies (where the rest mass of the particle may be neglected with respect to its kinetic energy) rapidity and pseudorapidity converge to the same value.

### 1.1.3 Cross section and luminosity

In particle physics, a cross section ( $\sigma$ ) is used to quantify the probability of occurrence of a given process. It describes the effective area of a collision. This allows for the use of the same SI units as for the classical geometric area ( $\text{m}^2$ ), but a more common unit is the barn (b), which is equal to  $10^{-28} \text{ m}^2$ .

Luminosity ( $L$ ) is a metric of a combination of accelerator properties. When multiplied by a cross section, this term gives the expected event rate ( $R$ ),

$$L\sigma = R. \quad (1.4)$$

Therefore, a higher luminosity leads to an increase in the likelihood of collisions resulting in a desired interaction. When integrated ( $L_{\text{int}} = \int_T L dt$ ), the integrated luminosity is proportional to the number of observed events over a given period  $T$ .

## 1.2 Standard Model

The Standard Model is a scientific theory quoted by many as being the most successful one of all time. It represents an amalgamation of theoretical descriptions of processes and phenomena studied over the past century built on three fundamental principles: quantum mechanics, relativity, and gauge invariance. An important property of this theory is its renormalisability, which resolves problems with infinities encountered in calculations and ensures consistency with the principles of quantum theory [1]. Whilst the Standard Model does have a few problems and is accordingly still considered to be incomplete, to this day it remains the best descriptor of the properties and interactions of the most fundamental building blocks of our universe. It has endured rigorous experimental testing and managed to predict phenomena decades before their eventual observation.

### 1.2.1 Forces

All observed forces can be classified as one of four fundamental interactions: electromagnetic, gravitational, strong, and weak. The approach to forces utilised in classical physics

cannot be applied in particle physics. Instead, particle interactions are described by quantum field theory (QFT) as interactions of quantum fields, which may be interpreted as an exchange of particles (see Sec. 1.2.2). It is important to remark that particle interactions are scale-dependent, as their coupling parameters vary with energy.

### **Electromagnetic interaction**

The electromagnetic interaction is by far the most common, being responsible for holding atoms together. It acts between all electrically charged particles. Its associated carrier is the photon ( $\gamma$ ), which, due to its zero rest mass, gives it an infinite range. The theory used to describe this interaction is quantum electrodynamics (QED).

### **Gravitational interaction**

The gravitational interaction is famously one of the shortcomings of the Standard Model. Its description through general relativity is not compatible with quantum theory, by extension neither with the Standard Model. However, this does not pose grave problems, since the very small strength of this force (compared with the other interactions) leads to its effects being negligible at energies achievable in current HEP experiments. Its intermediate particle, the graviton, has never been observed directly. Similarly to the photon, it is proposed to be massless, which explains the infinite range of gravity. Mass (or energy) acts as the 'gravitational charge' for this interaction.

### **Weak interaction**

The weak interaction acts between all fermions and is primarily responsible for decays, which are characterised by the emission of neutrinos. It is carried by three particles, the  $W^\pm$  and  $Z^0$  bosons, which are very massive. In consequence, it is limited only to very short distances and does not present itself at macroscopic scales. Due to the non-zero charge of the  $W$  boson, this interaction is the only one permitting particle flavour changes.

### **Strong interaction**

As its name suggests, the strong interaction is (relatively) the strongest of the four forces. It is responsible for binding nucleons in atomic cores as well as quarks in the nucleons themselves. The atomic nucleus is the maximum limit of its range and, similarly to the weak force, it is not observed macroscopically. It can act between particles carrying a colour charge. Its intermediate particles, gluons ( $g$ ), also carry this charge, ergo are able to interact amongst themselves. The theory behind this interaction is called quantum chromodynamics (QCD). One of its peculiarities is the fact that the strength of this interaction rises with the distance between interacting particles, leading to a phenomenon called colour confinement. The implications of QCD and the strong interaction are covered in more detail in Chapter 2.

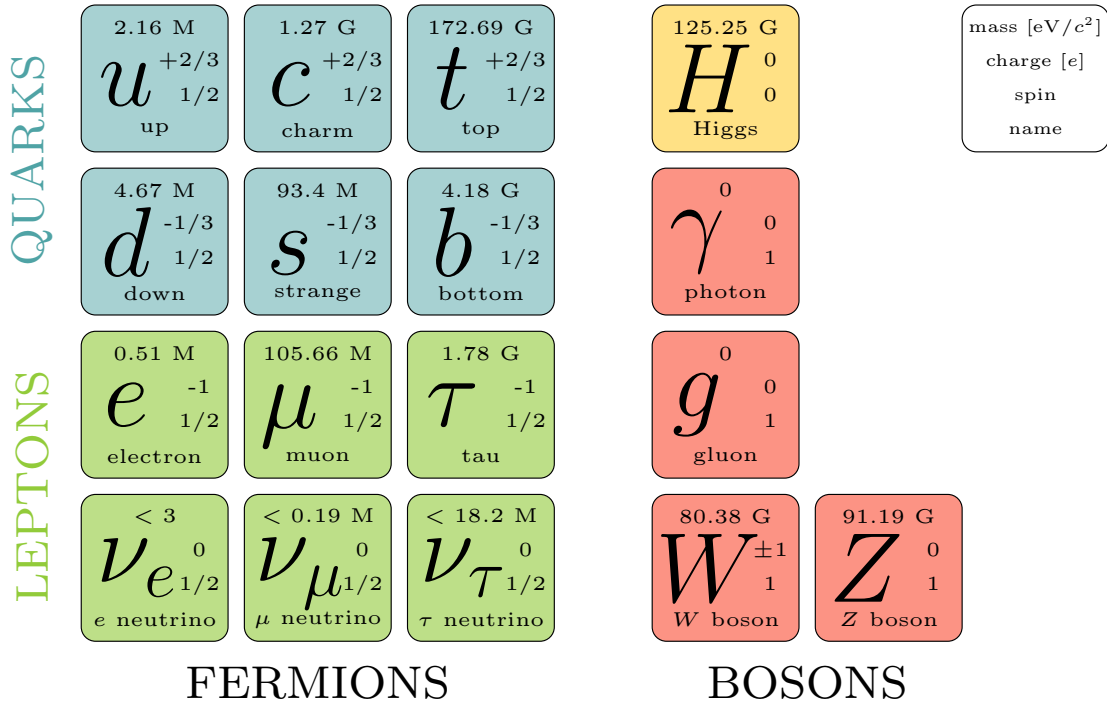


**Figure 1.1:** Diagram showing the classification of elementary particles in the Standard Model along with their basic properties. Adapted from Ref. [2], values updated from Ref. [3].

### 1.2.2 Particles

The Standard Model divides elementary particles into distinct groups on the basis of their spin. For an illustration of this division, see Fig. 1.1. Fermions are the fundamental building blocks of all observable matter in the universe and undergo interactions through gauge boson exchanges.

#### Fermions

Fermions are particles with spin  $1/2$ . Thus, Pauli's exclusion principle applies to them and no two fermions can occupy the same quantum state within a system. They are separated into three generations and further subdivided into two groups: quarks and leptons.

In total, there are six flavours of quarks (the up, down, charm, strange, top, and bottom). All quarks have been assigned a fractional electromagnetic charge. They also carry a non-zero colour charge and so, by themselves, do not form a 'white' or colourless particle. This, according to a postulate of QCD, makes them freely unobservable (see Sec. 2.1).

Leptons form the second group of fermions consisting of the electron, muon, tauon, and their respective neutrinos. As opposed to the quarks, leptons do not carry colour charges and as a consequence cannot enter into interactions via the strong force. Except for their mass, the charged leptons ( $e$ ,  $\mu$ , and  $\tau$ ) have very similar properties. Neutrinos are not electromagnetically charged. As mentioned previously, they are produced in decays through the weak interaction. Whilst they are very common, they rarely interact with surrounding matter. Neutrino mass is also one of the problems of the Standard Model. Theoretically, they are considered to be massless. Conversely, experiments and measure-

ments point to a phenomenon called neutrino oscillations, which can be explained only if a non-zero (albeit small) mass is allowed.

## Bosons

Bosons are particles with an integer value of spin and are therefore not subject to the Pauli exclusion principle. The aforementioned force carriers ( $\gamma$ ,  $g$ ,  $W^\pm$  and  $Z^0$ , also known as gauge bosons) all have spin 1 (thus are called vector bosons), while the hypothetical graviton is proposed to have spin 2 (making it a tensor boson) [3].

In the form of so-called virtual particles, gauge bosons are responsible for the mediation of forces. Virtual particles cannot be observed directly. The energy of a real observable photon is  $E = pc$  (considering  $m = 0$ ), whereas the same does not apply for an unobservable virtual photon (meaning that a virtual photon has non-zero mass). The respective masses of gauge bosons are directly tied to the range of the forces they mediate, as Heisenberg's uncertainty principle also applies to virtual particles and their mass (or rather energy  $\Delta E$ ) is tied to their lifetime ( $\Delta\tau$ ) through

$$\Delta E \Delta\tau \geq \frac{\hbar}{2}. \quad (1.5)$$

Being the only elementary particle with spin 0, the Higgs boson is the sole representative of the fundamental scalar boson category. It is not per se a force carrier, but it does mediate interactions of particles with the Higgs field. It is through this interaction that particles gain rest mass. Not all of them interact with this field, giving rise to massless particles such as photons, gluons, or the proposed gravitons.

## Hadrons

Hadrons are composite particles made up of quarks, most often in the form of a quark-antiquark pair forming a meson, or a triplet of quarks forming a baryon. However, these so-called valence quarks are not the only constituents of hadrons. Per Feynman's parton model, they are accompanied by a sea of ephemeral quark-antiquark pairs as well as virtual gluons, which bind the particles together. The constituents' colour charges cancel out and fractional EM charges add to an integer value. Hadrons can consequently be observed, although most are short-lived.

At present, the proton ( $uud$ ) is considered to be the only stable hadron. More accurately, a decay of a free proton has never been observed, and it is accordingly presumed to have a half-life longer than the current age of the universe. The neutron ( $udd$ ) is stable only when bound in an atomic core with other nuclei, otherwise it decays into a proton through  $\beta$  decay.

## The $\rho$ vector meson

Of particular interest to this thesis is the  $\rho$  meson. It forms an isospin ( $I$ ) triplet of particles varying in their electric charge, which in itself stems from their differing quark composition:  $\rho^+$  ( $u\bar{d}$ ),  $\rho^-$  ( $d\bar{u}$ ), and  $\rho^0$  ( $(u\bar{u} - d\bar{d})/\sqrt{2}$ ). This particle was discovered in 1961 by scientists from BNL during their studies of low-momentum-transfer  $\pi\pi$  events. A

strong dominance of the  $I = 1$  scattering state was observed, and the deduced scattering cross section indicated a peak at  $m \approx 750 \text{ MeV}/c^2$  [4].

As attested by more current measurements, the mass of the  $\rho$  meson is approximately  $(769.2 \pm 0.9) \text{ MeV}/c^2$ . This value is slightly different for the charged and neutral mesons, but interestingly, it also varies depending on the method of production of this particle (with the stated value given specifically for photoproduction of the neutral  $\rho$  state) [3]. It is frequently referred to as  $\rho(770)$ , signifying an accepted 'average' value. As a spin-1 particle, it is a vector meson.

The  $\rho$  is not stable and has a resonance width measured at  $\Gamma = (151.5_{-2.1}^{+1.9}) \text{ MeV}/c^2$  (again specifically for photoproduced neutral mesons). The lifetime of an unstable particle is inversely proportional to this value as  $\tau = \hbar/\Gamma$ . Therefore, in approximately  $4.3 \cdot 10^{-24} \text{ s}$  after its creation, the  $\rho$  decays, almost exclusively into pairs of pions:

$$\rho^0 \rightarrow \pi^+\pi^- \quad \text{and} \quad \rho^\pm \rightarrow \pi^\pm\pi^0 \quad (1.6)$$

for the neutral and charged meson, respectively. Other decays are possible but negligible, with their probabilities being orders of magnitude smaller than these primary modes [3].

## Chapter 2

# Basics of QCD

Quantum chromodynamics (QCD) is a quantum field theory utilised for the description of the behaviour of quarks in hadronic matter. Initially put forth in the 1970s, this non-abelian gauge theory based on the  $SU(3)$  colour symmetry group has managed to accurately explain certain phenomena observed in experiments. Several practical implications of QCD will be discussed in this chapter. Unless stated otherwise, the presented information is summarised from Ref. [1].

### 2.1 Colour

When the theoretical aspects of the quark model were being put together, a problem arose, as there were experimentally confirmed particles, whose proposed composition was in direct opposition to the Pauli exclusion principle. An example may be the  $\Omega^-$  baryon, which consists of three  $s$ , presumably identical, quarks. To resolve this violation, it was suggested that quarks in fact carry yet another quantum number, through which they may be distinguished and the seeming conflict be resolved. This new particle characteristic was called colour. As there can be up to three 'identical' quarks inside a baryon, three colours, usually denoted red, green, and blue, were proposed (correspondingly with three anticolours: antired, antigreen, and antiblue). Several experimental observations supported this claim.

Colour charge acts as the source of the chromodynamic force, similarly to how the electric charge is a source of the electromagnetic force. The carriers of the strong interaction, gluons, also carry colour (or rather a combination of a colour and an anticolour). All interactions mediated by them thus effectively change the colour of the individual quarks (see Fig. 2.1), but the total colour of a system is always conserved. This also generates their own colour fields and allows them to interact amongst themselves.

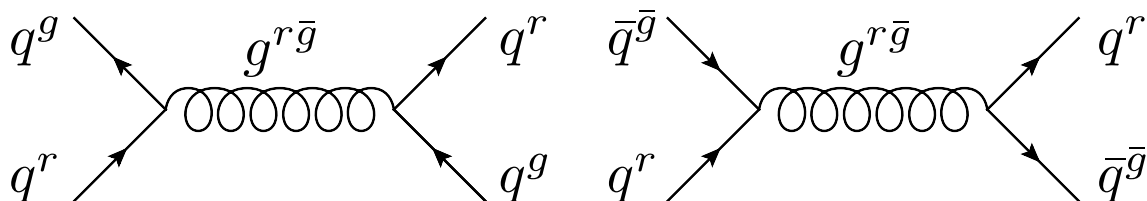


**Figure 2.1:** Diagram of quark interactions via a gluon exchange. Adapted from Ref. [1].

Colour has another profound impact on hadronic matter in that it dictates the observability of particles. According to a postulate of QCD, all observable hadrons are colour singlets. In a more practical wording, in order for a particle to be observable, the colours of its constituents must cancel out, leaving a colourless hadron. This is achievable for particles with a  $q\bar{q}$  or  $qqq$  configuration, which are the already introduced mesons and baryons, respectively. Theoretically possible are also combinations of  $q\bar{q}q\bar{q}$  and  $q\bar{q}qqq$ , tetra- and pentaquarks. Under 'standard' conditions, it is therefore impossible to observe quarks separately. This effect is known as colour confinement.

## 2.2 QCD coupling constant

The coupling constant (commonly denoted  $\alpha$ ) is an important parameter in QFT, as it effectively describes the strength of an interaction. A non-trivial fact is that the value of this constant depends on the scale at which it is examined. Several key characteristics of the strong interaction stem directly from the behaviour of its coupling constant  $\alpha_S$ , which is perhaps best illustrated in comparison with that of  $\alpha_{EM}$ , the coupling constant of the electromagnetic interaction.

QED experiments show that the size of  $\alpha_{EM}$  rises with decreasing distance and conversely falls with increasing distance, converging to the well-known value of  $\alpha_{EM} \approx 1/137$ . The behaviour of the QCD coupling constant is somewhat reversed, as  $\alpha_S$  is small for small distances and grows as they increase. This is important e.g. for DIS experiments (discussed in the following section), as when observed at large energies (small distances), the force binding quarks in hadrons is very small, and they may, for short intervals of time, be considered as essentially free particles (asymptotic freedom). On the opposite side of the distance spectrum, the strength of this interaction is very large. This presents an explanation for the aforementioned colour (quark) confinement phenomenon. To physically separate a constituent quark from a hadron, the interquark forces would have to be overcome. However, as their strength rises with distance, it is simply not possible to ever meet such a criterion. Beyond a certain point, it becomes energetically more efficient to 'pull' a quark-antiquark pair from vacuum and subsequently create two separate colourless particles.

A useful theoretical tool for examining problems in QFT is perturbative theory. In a manner similar to the Taylor series expansion of functions, it presents a possibility of simplification of the otherwise complicated (and often unsolvable) computational problems. The feasibility of this method is nevertheless reliant on the size of the coupling constant ( $\alpha$ ), as the terms of the series include increasing powers of  $\alpha$ . If the constant is sufficiently small ( $\alpha \ll 1$ ), terms beyond a certain power of the coupling constant may be omitted and the infinite sum thus be drastically reduced. This is not viable for large values of  $\alpha$ , as the higher-order terms grow in importance instead of losing it. It is therefore possible to utilise this approach only in high-energy QCD processes.

## 2.3 Deep-inelastic scattering experiments

Deep-inelastic scattering (DIS) experiments were historically very important, as they provided the very first glimpse into the inner structure of nucleons. This was generally achieved by studying the scattering of electrons off protons, with an exchanged virtual



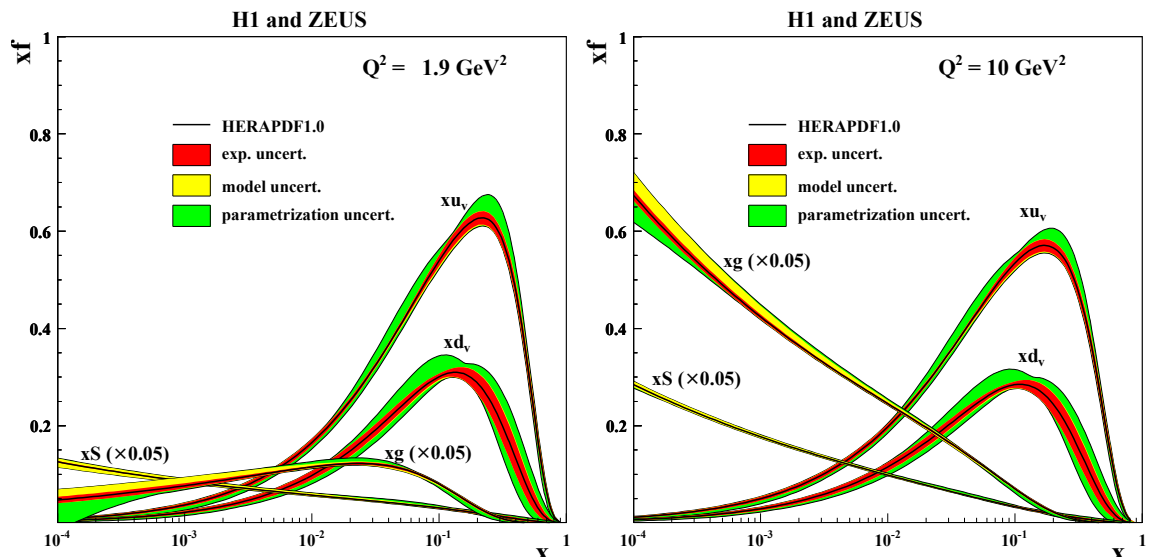


**Figure 2.2:** Parton distribution functions of proton constituents measured by the H1 and ZEUS collaborations at  $Q^2 = 1.9 \text{ GeV}^2$  (left) and  $Q^2 = 10 \text{ GeV}^2$  (right). Depicted are contributions from the valence up ( $xu_v$ ) and down ( $xd_v$ ) quarks alongside the sea quarks ( $xS$ ) and gluons ( $xg$ ), the latter two of which are scaled by a factor of 0.05. Adapted from Ref. [6].

photon serving as a probe. Since the interaction is electromagnetic, only the charged quark densities may be studied in this manner. Distributions of gluons must be determined by comparing data gathered at different energetic scales, often causing great theoretical uncertainties [5]. Direct probing of gluons requires an alternative approach, such as photoproduction, which will be further discussed in Sec. 3.2.

Today, nucleons are considered to be a collection of three valence quarks accompanied by gluons and sea quarks and antiquarks. These partons can be described using parton distribution functions (PDFs, see Fig. 2.2)  $f(x, Q^2)$ , which are characterised by two variables, Bjorken  $x$  and virtuality ( $Q^2$ ).

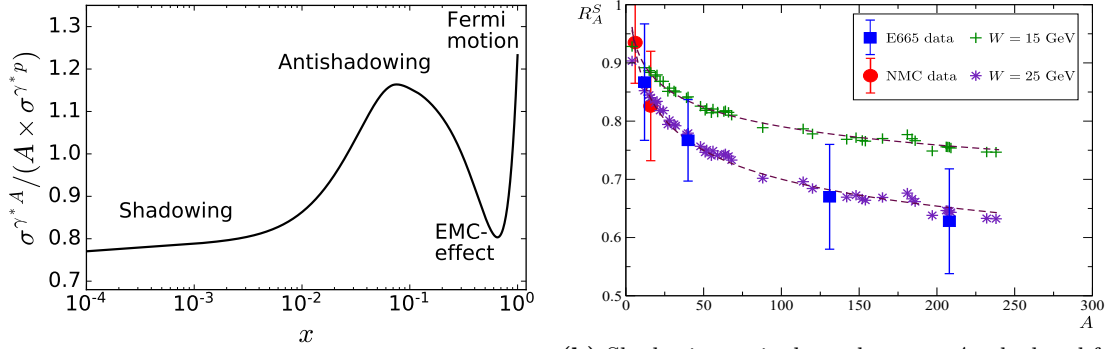
In the infinite momentum frame, the Bjorken  $x$  variable may be interpreted as the fraction of the total hadron (nucleon) momentum carried by one of its constituents. It is usually defined as

$$x = \frac{Q^2}{2pq}, \quad (2.1)$$

where  $p$  and  $q$  are the four-momenta of the incident particle (electron) and the exchanged virtual particle (photon), respectively, and virtuality  $Q^2 \equiv -q^2$  represents the square of transferred momentum. Virtuality sets the scale of the interaction and may be thought of as the 'resolution' of the virtual particle probe.

### 2.3.1 Saturation

Continuing with the intuitive analogy of a microscope resolution, reaching higher probe virtualities (shorter wavelengths) allows for a more detailed look into the structure of nucleons. The dominance of low- $x$  gluons and sea quarks for higher  $Q^2$  is apparent from Fig. 2.2. With increasing virtuality, even more low- $x$  partons would be observed, resulting from the probe's ability to discern various QCD sub-processes (such as gluon splitting and self-interaction). Nonetheless, it is thought to be impossible for their number to



(a) Cross section ratio measuring  $x$ -dependent nuclear effects on PDFs as seen in DIS experiments. Taken from Ref. [5].

(b) Shadowing ratio dependence on  $A$  calculated for centre-of-mass energy of  $W = 15$  and  $25$  GeV compared with experimental data from the NMC and E665 collaborations. Adapted from Ref. [8].

**Figure 2.3:** Nuclear effects on PDFs and shadowing  $A$ -dependence.

grow indefinitely with progressively smaller  $x$  values, as the total hadron phase space is finite. A limit on this rise presents itself upon reaching the state of gluon saturation. This is described theoretically as a point of dynamic equilibrium between gluon splitting and recombination, but this behaviour has not been conclusively demonstrated experimentally.

### 2.3.2 Nuclear shadowing

Experimental data show that partons are affected by their environment. PDFs for nucleons bound in nuclei are not equal to those describing a free nucleon, signifying a sensitivity to the proximity of other partons within the nucleus. In fact, several modifications (both diminishing and amplifying) have been observed, occurring at different values of  $x$  (see Fig. 2.3a). For low- $x$  values, parton densities are suppressed. This phenomenon is known as shadowing and is particularly prevalent in the high-density environments of heavy nuclei. Measurements indicate that the shadowing effect (i.e. the PDF suppression) increases with increasing  $A$  (nucleon number) of the studied nuclear species [7]. This is illustrated in Fig. 2.3b.

## Chapter 3

# Ultra-peripheral collisions and photoproduction

The initial geometry of a collision has a profound impact on subsequent interactions and particle production. Centrality is an important parameter for the study of heavy-ion collisions. In simple terms, it describes the degree of overlap between the two colliding ions, which dictates the number of nucleons that may participate in the collision. It is characterised by the impact parameter ( $b$ ) between the two colliding nuclei, defined as the distance between their centres in the plane transverse to the beam axis. Depending on its size in relation to the radii of colliding ions, collisions may be categorised into central, peripheral, and ultra-peripheral.

Ultra-peripheral collisions (UPCs) are a common occurrence in particle colliders. In this process, the two incident particles effectively miss each other, since they approach at an impact parameter greater than the sum of their radii (see Fig. 3.1). This suppresses hadronic interaction via the strong force, due to its limited range, but they may still interact electromagnetically through their electromagnetic fields.

Several processes may arise from interactions in UPCs. Generally, they are divided into photon–photon and photonuclear events. Of the latter category, exclusive vector meson photoproduction has garnered particular interest amongst the scientific community and is also the primary subject of this work. As such, it will be presented in more depth in the following sections.

### 3.1 Photon flux

From Fermi’s equivalent photon method, which was later expanded to cover relativistic ions by Weizsäcker and Williams, the electromagnetic fields surrounding the incident ions may be treated as fluxes of virtual photons [9]. Their intensity is proportional to  $Z^2$  (square of the atomic/proton number) of the nucleus, which leads to very high values for symmetric A–A collisions of heavy ions. The photons may also be considered quasi-real, since their virtuality is limited by the size of the emitting nucleus as  $Q^2 \leq \hbar^2/R_A^2$ , where  $R_A \approx 1.2A^{1/3}$  fm is the radius of a nucleus with mass (nucleon) number  $A$  [5].

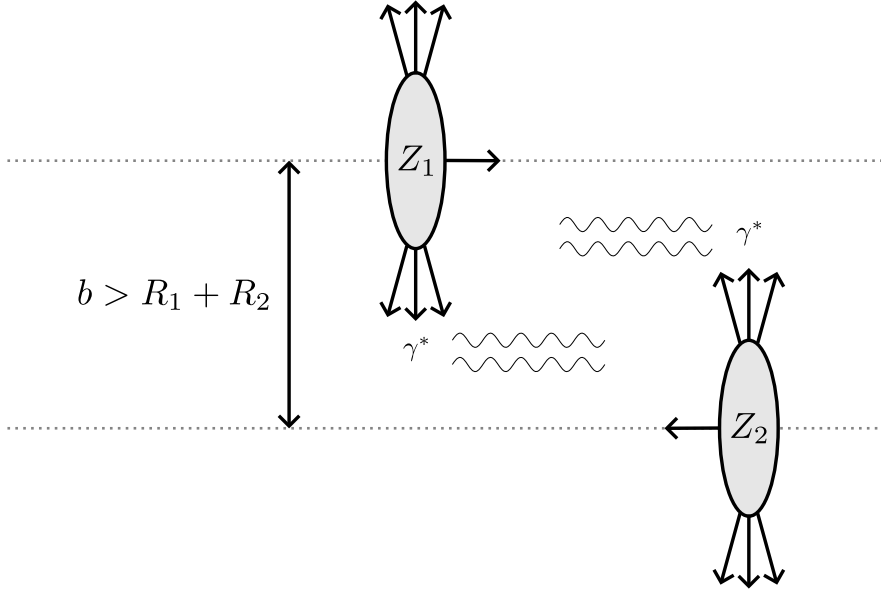


**Figure 3.1:** Schematic of an ultra-peripheral collision between two nuclei. Highlighted is the impact parameter ( $b$ ), which is larger than the sum of the two nuclear radii. Of note is also the particular pancake-like shape of the nuclei and their emitted electromagnetic fields (represented by fluxes of virtual  $\gamma^*$ ), which are both deformed due to Lorentz contraction along the beam direction.

In a semi-classical description, the photon flux per unit area for a point charge is given by

$$n(k,b) = \frac{\alpha Z^2}{\pi^2 b^2} x^2 \left[ K_1^2(x) + \frac{1}{\gamma} K_0^2(x) \right], \quad (3.1)$$

where  $k$  is the photon energy in the target nucleus frame ( $k \approx 2\gamma^2 \hbar c / R_A$  [5]) with Lorentz factor  $\gamma$ , and  $K_{0,1}$  are Bessel functions with variable  $x = kb/\gamma$ . For  $b > b_{\min} \equiv R_1 + R_2$  (so-called hard sphere approximation), this expression may be integrated over the impact parameter plane, resulting in

$$n(k) = \frac{2\alpha Z^2}{\pi} \left[ x_{\min} K_0(x_{\min}) K_1(x_{\min}) - \frac{x_{\min}^2}{2} (K_1^2(x_{\min}) - K_0^2(x_{\min})) \right], \quad (3.2)$$

where  $x_{\min} = kb_{\min}/\gamma$ . This can be related to the total photon flux from nucleus A by inputting the appropriate values of  $\gamma$  and  $Z$  into

$$N_{\gamma/A}(y,M) = k \left. \frac{dn(k)}{dk} \right|_A, \quad (3.3)$$

where  $M$  and  $y = \ln(2k/M)$  are the mass and rapidity of the final-state vector meson [10]. Several examples of these parameters are presented in Tab. 3.1. For an ion with proton number  $Z$  and nucleon number  $A$ , the Lorentz  $\gamma$  factor may be obtained as

$$\gamma = \frac{Z}{A} \frac{E_{\text{beam}}}{m_p}, \quad (3.4)$$

since the beam energy is proportional to the mass of a proton through  $E_{\text{beam}} = \gamma m_p$ . The  $Z/A$  factor accounts for the fact that only the charged nucleons (protons) are accelerated.

nucleus	$Z$	$A$	$E_{\text{beam}}$ [TeV]	$\gamma$
H	1	1	6.80	7247.37
Pb	82	208	6.80	2857.13
Xe	54	129	6.50	2899.94
O	8	16	6.80	3623.68

**Table 3.1:** Calculated Lorentz boost factors for particle beams accelerated in the LHC. Utilised values of proton and nucleon numbers ( $Z, A$ ), and particle beam energies ( $E_{\text{beam}}$ ) are in accordance with those presented in Sec. 4.2.2.

## 3.2 Exclusive vector meson photoproduction

As stated above, exclusive vector meson photoproduction is an electromagnetic photonuclear process, during which a photon emitted by either of the two incident nuclei interacts with the other nucleus and produces a vector meson (e.g. a  $\rho, J/\psi$ , etc.). This may be written as

$$A + A \rightarrow A + A + V, \quad (3.5)$$

where  $A$  represents the colliding heavy ions and  $V$  is the final-state vector meson. For an illustrative schematic of this process (production of  $\rho^0$ , followed by its 2-pion decay), see Fig. 3.2. Being exclusive, this process has a very clear experimental signature, with only the decay products of the vector meson present in the detector.

The differential photoproduction cross section for a symmetric heavy-ion UPC can be expressed as

$$\frac{d\sigma_{AA}(y)}{dy} = N_{\gamma/A}(y, M)\sigma_{\gamma A}(y) + N_{\gamma/A}(-y, M)\sigma_{\gamma A}(-y), \quad (3.6)$$

where  $M$  and  $y$  are again the final-state vector meson mass and rapidity and  $\sigma_{\gamma A}(y)$  is the corresponding photonuclear cross section. Either one of the incident nuclei can act as the source of the interacting photon, which leads to an ambiguity expressed by the two terms for opposite rapidities. The photonuclear cross section is sensitive to nuclear gluon distributions. This is one of the main motivations for the study of photoproduction, as it provides insight into several associated phenomena, such as nuclear shadowing or gluon saturation, which were briefly described in the previous chapter.

Photoproduction may be coherent (during which the photon interacts coherently with the entire nucleus, setting a constraint on the transferred transverse momentum with  $p_T < \hbar/R_A$  [5]) or incoherent (with generally higher final-state transverse momenta accompanied by a breakup of the 'target' nucleus). Of note is also the possibility of coherent photoproduction with nuclear breakup, which is caused by an independent secondary excitation of the target nucleus due to the intense photon fluxes [10]. This is particularly the case for UPCs of high- $Z$  heavy ions (such as Pb) and may be used experimentally, as will be seen in Chapter 5.

Several models attempt to describe the process of photoproduction and predict the associated cross sections. They generally follow three differing approaches and as such may be grouped together into models based on the (generalised) vector dominance model (GVDM), leading-order perturbative QCD, or the colour dipole model [10]. LO pQCD models are perhaps the most illustrative, as they clearly show the  $\sigma$  dependence on the square of the gluon distributions within nuclei, but this work will further discuss only the GVDM-based STARlight model.

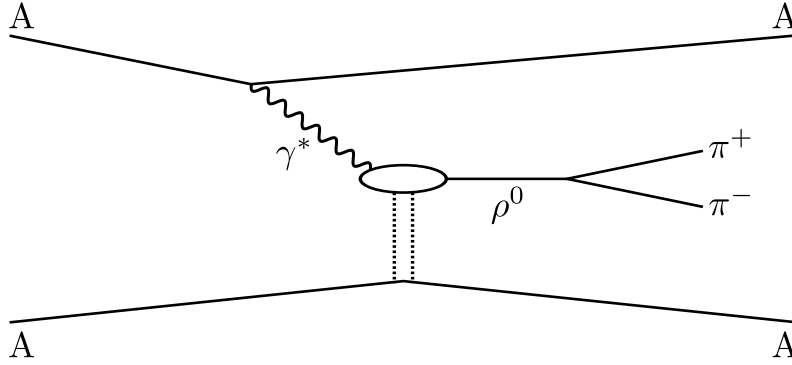


**Figure 3.2:** Schematic of  $\rho^0$  photoproduction in a heavy-ion (A) UPC followed by its 2-pion decay.

### 3.2.1 STARlight model for coherent photoproduction of $\rho$

The model developed by S. R. Klein and J. Nystrand, as described in Ref. [11] (from which the information presented in this section is taken) and further implemented in their STARlight program [12] (a Monte Carlo generator) is based on GVDM. It describes photoproduction as a photon–meson and photon–Pomeron interaction, both of which contribute to the cross section in proportion to the centre-of-mass energy of the system.

The photon flux is obtained similarly to the general method already introduced in Sec. 3.1, with a notable difference in the restriction of hadronic interactions. As opposed to the aforementioned hard sphere approximation, this model calculates the probability of having no hadronic interactions, which follows a Poisson distribution related to the overlap function  $T_{AA}(b)$  and the total nucleon–nucleon interaction cross section  $\sigma_{NN}$  as

$$P_{0H}(b) = \exp(-T_{AA}(b)\sigma_{NN}). \quad (3.7)$$

This is then used as a modulation factor during the integration of the flux density, giving a more accurate total photon flux value.

For the prediction of photoproduction cross sections, the model relies on input of  $\sigma(\gamma p \rightarrow Vp)$  data obtained by the HERA experiment. These cross sections can be parameterised as

$$\left. \frac{d\sigma(\gamma p \rightarrow Vp)}{dt} \right|_{t=0} = b_V (XW^\varepsilon + YW^{-\eta}). \quad (3.8)$$

$-t$  represents the square of transferred four-momentum and  $W$  the centre-of-mass energy of the proton–proton system. All other parameters are constants determined from data fitting.  $X$  and  $\varepsilon$  are related to the Pomeron exchange contribution to the cross section, which slowly rises with  $W$ , while  $Y$  and  $\eta$  describe the meson exchange contribution. This second term falls rapidly with increasing  $W$  and is suppressed for heavier vector mesons (such as  $\phi$  or  $J/\psi$ ). Particularly for the  $\rho^0$ , the following values are used:  $b_V = 11 \text{ GeV}^{-2}$ ,  $X = 5.0 \mu\text{b}$ ,  $\varepsilon = 0.22$ ,  $Y = 26.0 \mu\text{b}$ , and  $\eta = 1.23$ .

Next, an eikonalisation technique and the optical theorem are used. From GVDM, the expression

$$\left. \frac{d\sigma(\gamma p \rightarrow Vp)}{dt} \right|_{t=0} = \frac{4\pi\alpha}{f_V^2} \left. \frac{d\sigma(Vp \rightarrow Vp)}{dt} \right|_{t=0} \quad (3.9)$$

may be written, relating the two cross sections through the fine-structure constant  $\alpha$  and an  $f_V$  factor describing the photon–vector meson coupling. Subsequent application of the

optical theorem gives the total Vp cross section

$$\sigma_{\text{tot}}^2(\text{Vp}) = 16\pi \left. \frac{d\sigma(\text{Vp} \rightarrow \text{Vp})}{dt} \right|_{t=0}, \quad (3.10)$$

which is then used in a Glauber calculation to find the total vector meson–nucleus cross section

$$\sigma_{\text{tot}}(\text{VA}) = \int [1 - \exp(-\sigma_{\text{tot}}(\text{Vp})T_{\text{AA}}(\vec{r}))] d^2\vec{r}. \quad (3.11)$$

Finally, the differential cross section for  $\gamma\text{A} \rightarrow \text{VA}$  is found using the optical theorem and GVDM:

$$\left. \frac{d\sigma(\gamma\text{A} \rightarrow \text{VA})}{dt} \right|_{t=0} = \frac{\alpha\sigma_{\text{tot}}^2(\text{VA})}{4f_V^2}. \quad (3.12)$$

This cross section, calculated for coherent  $\rho$  production on a gold target, is shown in Fig. 3.3.

The total photonuclear cross section is

$$\sigma(\gamma\text{A} \rightarrow \text{VA}) = \left. \frac{d\sigma(\gamma\text{A} \rightarrow \text{VA})}{dt} \right|_{t=0} \int_{t_{\text{min}}}^{\infty} |F(t)|^2 dt, \quad (3.13)$$

where the nuclear form factor  $F(t)$  is the Fourier transform of the nuclear density profile, which is gained through approximation. For sufficiently narrow resonances, the lower integration limit is  $t_{\text{min}} = (M_V^2/4k)^2$ , but the same cannot be used for the  $\rho$ . Instead, the  $\rho$  cross section is calculated with a Breit-Wigner resonance,

$$\frac{d\sigma}{dM_{\pi\pi}} = \frac{2}{\pi} \frac{\sigma_0 \Gamma_\rho M_\rho M_{\pi\pi}}{(M_{\pi\pi}^2 - M_\rho^2)^2 + \Gamma_\rho^2 M_\rho^2}. \quad (3.14)$$

$M_{\pi\pi}$  is the invariant mass of the final state,  $M_\rho$  the resonance pole position,  $\sigma_0$  the total cross section without phase space corrections and  $\Gamma_\rho$  the Breit-Wigner width with phase space corrections. This cross section is illustrated in Fig. 3.4.

Integration of the photonuclear cross section over the photon spectrum gives the total cross section

$$\sigma(\text{AA} \rightarrow \text{AAV}) = \int_0^\infty \frac{dN_\gamma(k)}{dk} dk \int_{t_{\text{min}}}^\infty \left. \frac{d\sigma(\gamma\text{A} \rightarrow \text{VA})}{dt} \right|_{t=0} |F(t)|^2 dt. \quad (3.15)$$

The predicted values are very large, especially for the lightest  $\rho$  meson, leading to high production rates. If the photon flux is not modulated by the no-hadronic-interaction probability and the discussed hard-sphere integration limit ( $b > 2R_A$ ) is used, the resulting rates reportedly increase by approximately 5%. Owing to such large cross sections, the probability of multiple interactions in a single UPC is not negligible and a significant number of vector meson pairs is expected to be produced, with even higher multiples also being possible.

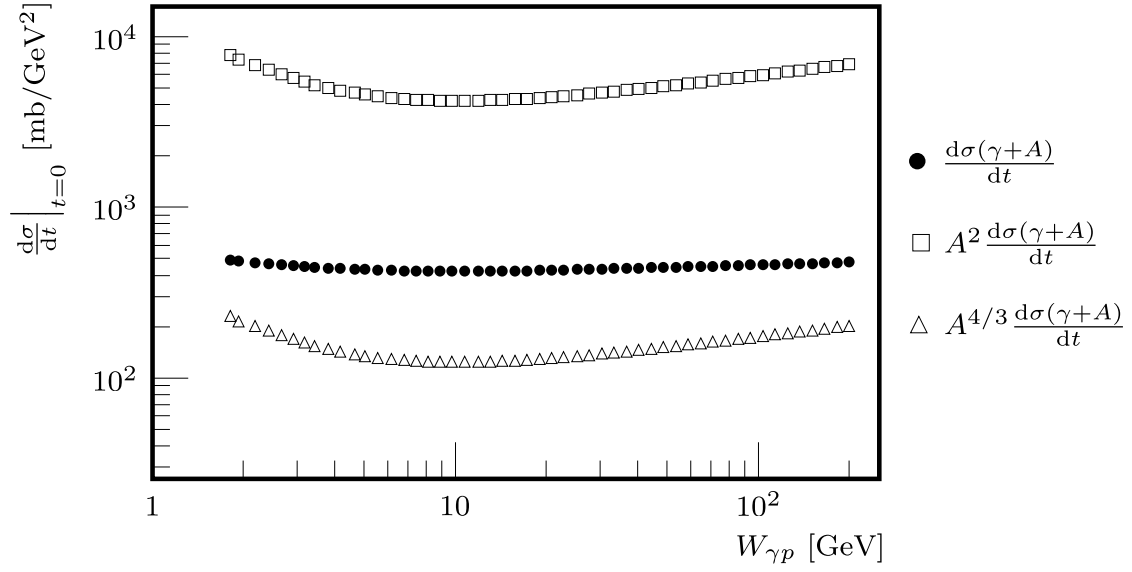


**Figure 3.3:** Plot of  $d\sigma/dt$  for coherent  $\rho$  production on a gold target as a function of centre-of-mass energy  $W_{\gamma p}$ . Also shown are the weak absorption ( $A^2$ ) and black disk ( $A^{4/3}$ ) scaling limits. Especially in the scaled plots, a minimum at  $W_{\gamma p} \approx 10$  GeV is apparent. This is the result of the transition from meson-dominated to Pomeron-dominated reactions. Adapted from Ref. [11].

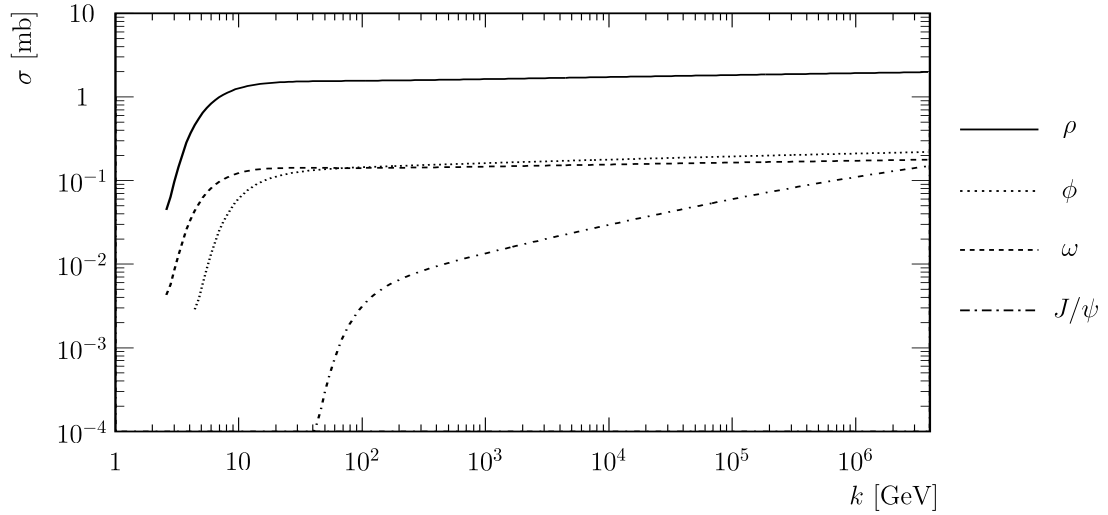


**Figure 3.4:** Photonuclear cross section of coherent production of vector mesons ( $\rho$ ,  $\phi$ ,  $\omega$ , and  $J/\psi$ ) on a gold target as a function of  $k$ , photon energy in the target nucleus rest frame. Adapted from Ref. [11].



## Chapter 4

# CERN, the LHC, and ALICE

Perhaps a surprising fact of HEP is that the study of the smallest features of the universe requires the building of some of the largest machines ever constructed by humanity. Amongst the best examples is CERN and its accelerator complex, which houses the largest particle accelerator in the world, the LHC. This organisation, its main accelerator, and the ALICE experiment are described in this chapter.

### 4.1 CERN

The European Organisation for Nuclear Research (CERN) was established in 1954. Since its inception, this international collaboration currently consisting of 23 member states (and several other non-member states) has become a world leader in fundamental research (mainly, but not exclusively) in the field of HEP [13]. It is one of the world's largest scientific facilities owing to its extensive state-of-the-art accelerator complex; see Fig. 4.1.

Although it is mostly known for its contributions to particle physics (in recent history notably the discovery of the Higgs boson), CERN's research has widespread applications in many other fields, including IT and medicine.

### 4.2 LHC

The Large Hadron Collider (LHC) represents the final stage in the chain of accelerators operated by CERN. Brought into service in 2008, this 27-kilometre-long accelerator underneath the border between Switzerland and France (utilising the tunnel left over after the dismantling of the LEP) remains to this day the largest and most powerful particle accelerator in the world. Its original goal was to produce the Higgs boson, which it accomplished successfully only a few years into its operation. Following this breakthrough, it continues working as a 'Higgs factory' producing more of these particles for their properties to be measured by various experiments, whilst also searching for supersymmetry, studying the quark-gluon plasma (QGP) and looking for signs of dark matter.

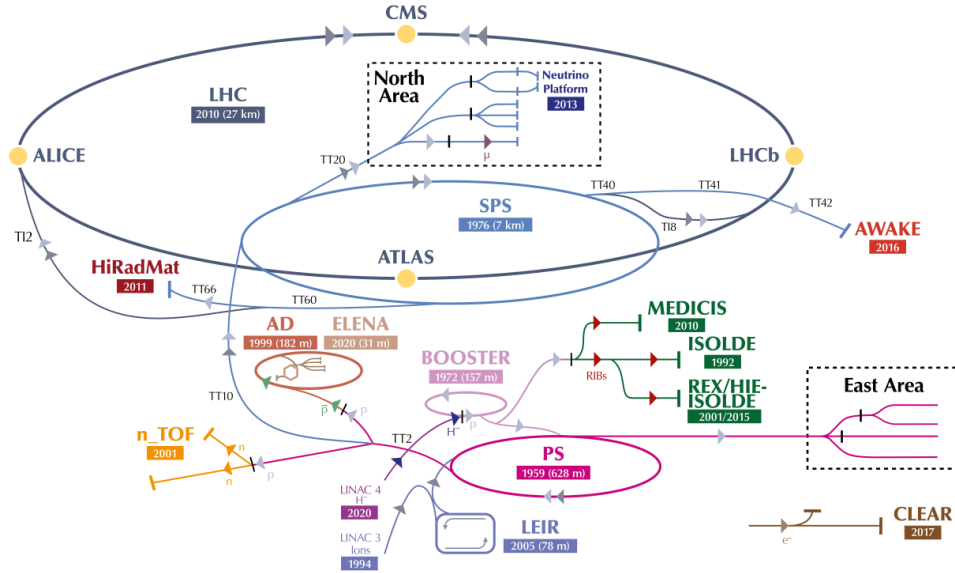


**Figure 4.1:** Diagram of the CERN accelerator complex as of 2022. Of note is the LHC, which houses the four biggest experiments of CERN: ALICE, ATLAS, CMS, and LHCb. Adapted from Ref. [14].

#### 4.2.1 Design and operation

To attain the required luminosity levels, the LHC was designed as a particle–particle collider (as opposed to a particle–antiparticle collider like its predecessor, LEP). This implies the need for two rings with counter-rotating beams. Due to space constraints, the LHC houses the two beam channels within the same structure. Its superconducting dipole magnet system was designed to generate nominal fields of 8.33 T. This requires the use of a cryogenic system based on superfluid helium, which cools the magnets to temperatures below 1.9 K. Vacuum systems provide insulation for the cryomagnets, the helium distribution system, and the beamlines themselves. Particle beams gradually pass through the entirety of the accelerator chain, reaching energies of up to 450 GeV in the SPS, upon which they are injected into the LHC and accelerated further using 400 MHz superconducting radio frequency cavities [15].

The LHC operates in Runs (periods of near-continuous particle collisions) interspaced by Long Shutdowns (LS), which are reserved for maintenance and system upgrades. Proton–proton collisions take up the majority of its operational time, with approximately one month every year reserved for heavy-ion collisions; see Fig. 4.2. The 2022 heavy-ion run was cancelled (only a Pb test run was performed) and the year-end technical stop (YETS) began earlier than usual. The next Pb–Pb run is scheduled for October 2023, promising 27 days of ion collisions with an estimated delivery of  $2.5\text{--}3.5\text{ nb}^{-1}$  of interactions to the experiments. Due to the ongoing energy crisis, there is a possibility of running at a 20% cut in physics time and adopting an extended YETS for the entire duration of Run 3 [16].

A major enhancement of several of the key systems of the accelerator, called the High-Luminosity Large Hadron Collider (HL-LHC), is currently in progress. The aim is to vastly increase the luminosity of the LHC (up to ten times the nominal design value) to continue producing statistically relevant amounts of data for decades to follow. This will be possible with the installation of new technologies, including newly designed magnets

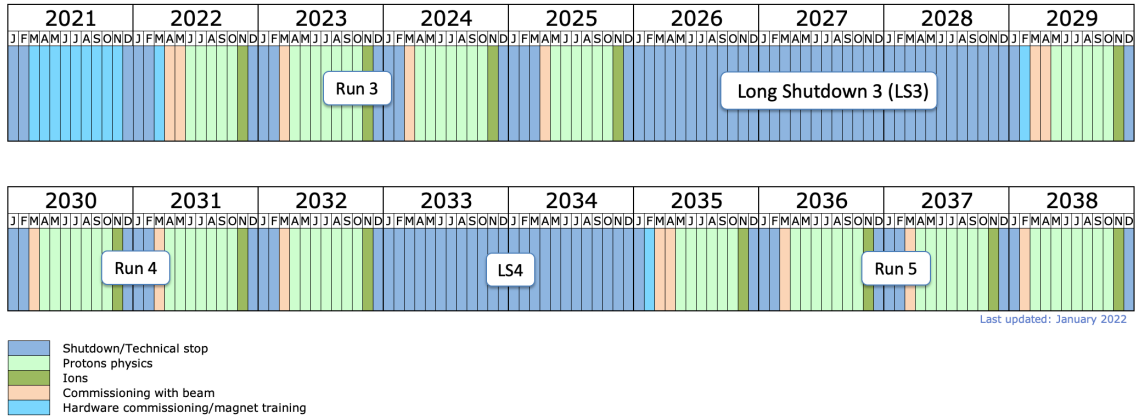


**Figure 4.2:** Projection of the LHC long-term operation schedule as of January 2022. Taken from Ref. [17].

with a strength of up to 12 T, compact superconductive RF cavities, improvements to beam collimation, etc. Several upgrades have already been made over LS2, whereas most are scheduled to be installed during LS3 [18].

#### 4.2.2 LHC collision systems

The initial LHC design accounted only for symmetric pp and Pb–Pb collisions. While they still remain the most extensively studied systems, the accelerator chain is capable of actuating collisions of other nuclear species. Over the two completed Runs, the LHC has to date provided collisions of four systems, an overview of which may be seen in Tab. 4.1.

system	year	$\sqrt{s_{NN}}$ [TeV]
pp	2009–2013	0.90, 2.76, 7.00, 8.00
	2015, 2017	5.02
	2015–2018	13.00
p–Pb	2013	5.02
	2016	5.02, 8.16
Pb–Pb	2010, 2011	2.76
	2015, 2018	5.02
Xe–Xe	2017	5.44

**Table 4.1:** Collision systems and their centre-of-mass energies per nucleon–nucleon collision ( $\sqrt{s_{NN}}$ ) studied by the LHC experiments in Runs 1 and 2. Taken from Ref. [19].

#### pp and Pb–Pb

As mentioned previously, proton–proton collisions constitute the vast majority of the active running time of the machine. The (fully stripped  $^{208}\text{Pb}^{82+}$ ) lead–lead heavy-ion programme was initially intended to supply data solely for the ALICE experiment, but eventually all the 4 major experiments began studying this collision system and the programme became exceedingly successful. Since its commissioning, the LHC has attained ever so greater beam energies and intensities. With the beginning of Run 3 in 2022,

proton collisions at 13.6 TeV were observed, followed shortly by lead nuclei collisions at  $\sqrt{s_{\text{NN}}} = 5.36$  TeV, both record-breaking values for the respective collision systems [20].

### **p–Pb**

Asymmetric collisions present several technical challenges for the operation of the accelerator complex. At CERN, the initial stages of the injector chain are separate for protons and lead ions, as they pass through different linear accelerators and primary synchrotrons (at present Linac4 + Booster for protons and Linac3 + LEIR for ions; see Fig. 4.1). Applying an appropriate filling scheme to obtain the same bunch pattern in both beamlines is also non-trivial and differs greatly from standard operations. Furthermore, the dipole field in both beam apertures of the LHC is identical, which leads to a difference in the speed and orbital period of the two dissimilar particle beams. The RF acceleration cavities can be operated independently during the injection, but their frequencies must be matched for collision data collection, in order to ensure that the collision points between bunches remain stationary. This imparts a limit on viable collision energies [21]. Nevertheless, proton–ion (p–A) collisions serve as an important benchmark for the interpretation of heavy-ion collision data and have been studied at the LHC several times, with p–Pb energies reaching up to  $\sqrt{s_{\text{NN}}} = 8.16$  TeV.

### **Xe–Xe**

During 2017, the SPS accelerated beams of  $^{129}\text{Xe}^{54+}$  nuclei for its fixed-target experiments. Since this presented a unique opportunity to study heavy-ion collisions of a new nuclear species, the beams were also injected into the LHC for an 18-hour run (6 h of physics data-taking) with a beam energy of  $6.5Z$  TeV (corresponding to  $\sqrt{s_{\text{NN}}} = 5.44$  TeV). The integrated luminosity delivered during this run was comparable to the very first month-long Pb ion run in 2010. The recorded data was used e.g. for the study of photoproduction (discussed in Chapter 5) and provided useful insights into beam cleaning and collimation efficiency [22].

The prospect of colliding lighter nuclei has been gaining traction with the ongoing HL-LHC upgrades and preparation for further Runs (4 and mainly 5). During collisions of heavy ions, ultra-peripheral EM interactions dominate the total cross section and lead to fast beam intensity degradation. As these effects scale with powers of  $Z$ , beams of lighter ions have longer lifetimes and the feasible integrated luminosities are expected to vastly surpass those obtainable with lead ions [22].

### **O–O and p–O**

Following the success of the Xe–Xe and p–Pb runs, a scenario for an approximately one-week-long  $^{16}\text{O}^{8+}$  programme has been proposed and is currently scheduled for 2024 [23]. Amongst the several motivations for the study of this particular collision system is its position as an ‘intermediate’ system capable of bridging the gap between the already observed proton and heavy-ion collision systems. Advantageous is also the fact that oxygen ions are readily available for injection into the accelerator chain, since oxygen serves as a support gas for the currently used lead ion source. Collisions of a new nuclear species could provide more insight into the collective behaviour of QGP in small systems, such as jet quenching and flow effects, or particle and light-nuclei production. A brief oxygen run

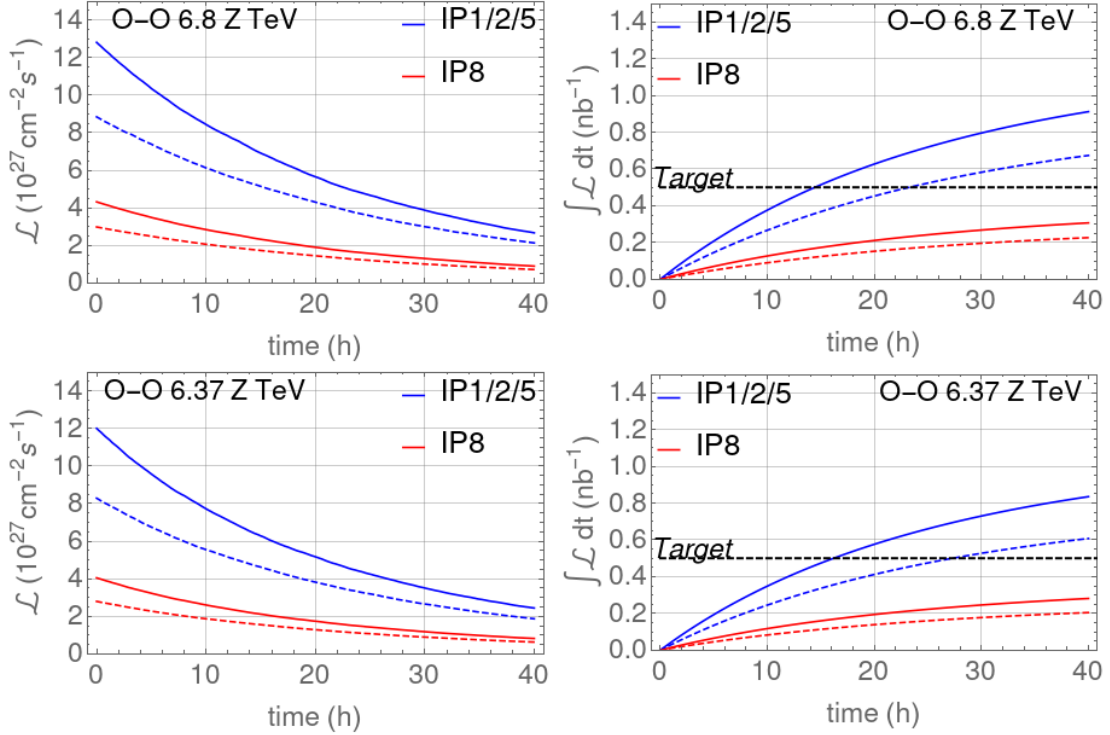


**Figure 4.3:** Simulated performance (instantaneous and integrated luminosities) for two of the proposed scenarios of an O–O run: 21 bunches with  $1.5 \cdot 10^9$  ions/bunch (dashed line), and 18 bunches with  $2.0 \cdot 10^9$  ions/bunch (solid line). Taken from Ref. [23]

would also enable new studies of diffractive processes and measurements of light vector meson production. Proton–oxygen collisions are of particular interest to astroparticle research, since they can improve the understanding of cosmic ray interactions with the atmosphere [24].

The expected integrated luminosity of the proposed O–O run is  $0.5\text{--}1.0 \text{ nb}^{-1}$ , which covers the requests from the ALICE, ATLAS, and CMS experiments. LHCb has expressed interest in p–O collisions with a total integrated luminosity of  $2 \text{ nb}^{-1}$  and running with reversed beams (O–p collisions) is currently not planned [25]. Several scenarios of different bunch configurations and beam energies have been considered to date. The beam energy has not been finalised as of the time of writing, the discussed values are on the order of  $6.37\text{--}7.00 \text{ Z TeV}$  (for oxygen ions, the beam energy is identical to the centre-of-mass energy per nucleon-pair collision  $\sqrt{s_{NN}}$ ) [24]. The latest luminosity projections for two of the considered fill scenarios are depicted in Fig. 4.3.

### 4.3 ALICE

Located at Point 2 of the LHC, ALICE (A Large Ion Collider Experiment) is one of the four main detectors at CERN. It is a general-purpose heavy-ion detector, which focuses on the study of QCD and the strong interaction, mainly through the observation of the quark-gluon plasma, a novel state of matter formed from deconfined elementary particles, which is produced in the extreme energy densities and temperatures of nucleus–nucleus collisions. To this end, ALICE studies primarily the collisions of lead ions, but data from other collision systems (lighter ions, proton–nucleus, and even proton–proton collisions)

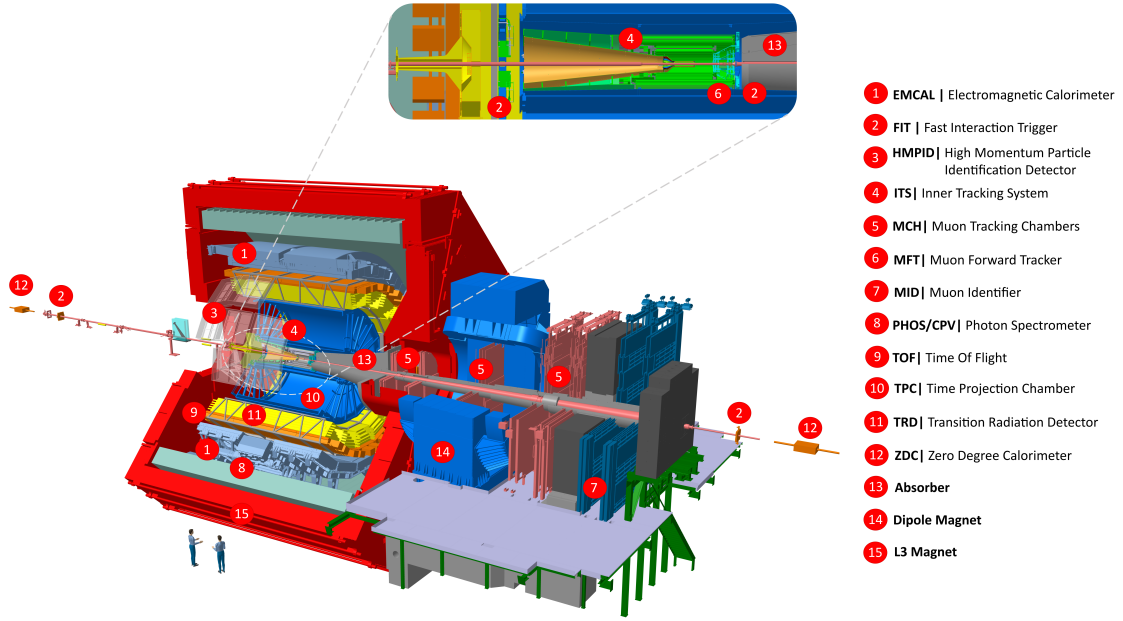


**Figure 4.4:** Diagram of the ALICE detector (as of Run 3) showing its subsystems. The central barrel section is enclosed within a large solenoid magnet (15, depicted in red), with the muon spectrometer extending out on the C side of the experiment. Taken from Ref. [27].

are also collected.

Several complementary subdetector systems constitute this detector. They were optimised for high momentum resolution and accompanying particle identification (PID) whilst coping with high particle multiplicities arising from heavy-ion collisions. In general, there are three distinct parts of the experiment: a central barrel section, which is kept in a 0.5 T magnetic field generated by a large solenoid magnet enclosing the structure, the muon spectrometer, and the forward detectors (the ZDCs, FIT, etc.) [26]. A schematic of the detector can be seen in Fig. 4.4.

With upgrades to the LHC following LS2 and ever-evolving detector technologies, ALICE underwent a major overhaul in preparation for Run 3. This consisted of changes to its core detectors (briefly touched upon in the following section) and the move to continuous readout mode, coupled with the introduction of a new event processing system with a redesigned Online–Offline software framework, which will be covered in more detail in Sec. 4.3.2 of this thesis. These improvements will enable recording of Pb–Pb collisions at rates of up to 50 kHz [27].

### 4.3.1 Detectors

A select few of ALICE’s subdetectors will be explored further. They were chosen because of their importance for previous photoproduction measurements (either directly or as triggers/vetoes) discussed in articles covered in Chapter 5 as well as the data analysis presented in Chapter 6. Information is taken from Refs. [26, 27], unless stated otherwise.

## ITS

The Inner Tracking System is the closest detector to the beam line (see Fig. 4.6). As such, it is responsible for the localisation of primary vertices, tracking, and PID of particles with momenta below  $200 \text{ MeV}/c$ .

Originally, it consisted of six layers of silicon detectors positioned coaxially along the beam pipe. The two innermost layers were made up of Silicon Pixel Detectors (SPDs), Silicon Drift Detectors (SDDs) were used for the following two, and the outermost layers were equipped with Silicon micro-Strip Detectors (SSDs). During several measurements, the SPD layers were used as trigger detectors.

**ITS2** During LS2, the ITS was upgraded to cope with the increased interaction rate expected in the following Runs. The new ITS2 is made up of 7 layers based on the ALPIDE sensor, with the goal of improving the precision of vertex reconstruction and the detection performance for particles with low  $p_T$ . The positions of all layers have been appropriately adjusted. The readout rates of the detector were enhanced to 50 kHz for Pb–Pb and 400 kHz for pp collisions, and the pseudorapidity coverage increased to  $|\eta| < 1.22$ .

## TPC

The Time Projection Chamber is a large cylindrical gas tracking detector enveloping the ITS(2). Its  $88 \text{ m}^3$  of total active volume are filled with a Ne-CO<sub>2</sub>-N<sub>2</sub> gas mixture (with a ratio of 90-10-5 parts) and separated into two halves by a central high-voltage electrode. For readout, primary electrons are transported to the end plates on either side of the detector.

During Run 1 and 2, multiwire proportional chambers formed the basis of the readout chambers. These were incompatible with the continuous readout mode and were therefore upgraded using GEM foil technology. The TPC is capable of covering a pseudorapidity range of  $|\eta| < 0.9$  (for full radial track length) at full azimuth.

## TOF

The Time-Of-Flight detector is an array of gaseous MRPC strip detectors surrounding the TPC. It supplements the properties of the other detectors within the central barrel, providing PID for the intermediate  $p_T$  range (up to  $4 \text{ GeV}/c$  for protons and  $2.5 \text{ GeV}/c$  for pions) for a similar pseudorapidity interval of  $|\eta| < 0.9$ . Coupled with the ITS and TPC, the three detectors allow for accurate reconstruction of tracks and vertices as well as measurements of ionisation energy loss for PID.

Minor adjustments to the TOF electronics were made in preparation for the Run 3 continuous readout mode.

## V0, AD, and FIT

The V0 was a small-angle detector composed of two arrays of scintillator counters positioned on each side (designated A and C) of the interaction point. Although it had several

functions, it mainly served as a trigger for other detectors in the central barrel. Through recording multiplicity, it also allowed for the estimation of centrality and determination of luminosity.

The ALICE Diffractive detector was part of the experiment during Run 2. It also was a 2-arm detector, with the two subdetectors following the standard naming convention. ADA was placed 18 m from the IP and covered a pseudorapidity interval of  $4.8 < \eta < 6.3$ , while the ADC was located 20 m from the IP and covered  $-7.0 < \eta < -4.9$ . Each of the subdetectors was composed of 8 scintillation cells arranged in two planes. As its name suggests, it served as a trigger for diffractive events [28].

Both V0 and AD were made redundant with the installation of the Fast Interaction Trigger (FIT, see Figs. 4.5 and 4.6) over the course of LS2, whose distinct sections supplanted their functionality. It will deliver minimum-bias triggering, monitoring of background and luminosity, collision timing and vertexing, and vetoing for ultra-peripheral and diffractive events [29].

**FV0** The V0 was replaced by the FV0 scintillator disc, providing minimum bias and multiplicity triggers, and monitoring background conditions. This detector is not separated into two arms as its predecessor, and the resulting space previously occupied by V0C was filled by the MFT. The disc is segmented into 5 concentric rings of plastic scintillator, which is the active element of the detector. It employs a new short-pulse light collection scheme, ensuring a 200 ps minimum-ionizing particle (MIP) time resolution and a uniform response across the detection surface.

**FDD** The Forward Diffractive Detector replaced the AD. The new subdetectors are placed 17 m and 19.5 m from the IP on the A and C side, respectively. Both stations consist of two layers of four segments of plastic scintillators. The use of materials with better timing response during its construction has led to a reduction of signal time width by approximately 11 ns [29]. Owing to its sensitivity, the FDD is ideal for tagging interactions with large rapidity gaps, such as ultra-peripheral collisions or diffractive processes.

**FT0** The FT0 is composed of two arrays of Cherenkov radiators coupled to MCP photomultipliers. The FT0-C is installed close to the IP (approximately 84 cm away) and houses a total of 112 radiators. The other 96 are mounted in the FT0-A, which lies 3.3 m away from the IP, close to the FV0. This detector achieves a single MIP time resolution of 25 ps.

## ZDCs

Zero-Degree Calorimeters are primarily used to estimate collision centrality. This is achieved by measuring the energy carried by spectator nucleons in the forward direction. They can also be used as triggers for van der Meer scans for luminosity determination [31]. Two sets of ZDCs are located on either side of the experiment, approximately 116 m from the IP. Since spectator protons are separated from neutrons by the magnetic systems of the LHC, each ZDC comprises two distinct and correspondingly spatially separated detectors. The ZDCs are quartz fibre calorimeters, relying on the production of Cherenkov radiation by the incident particles. They are subject to intense radiation and are therefore placed



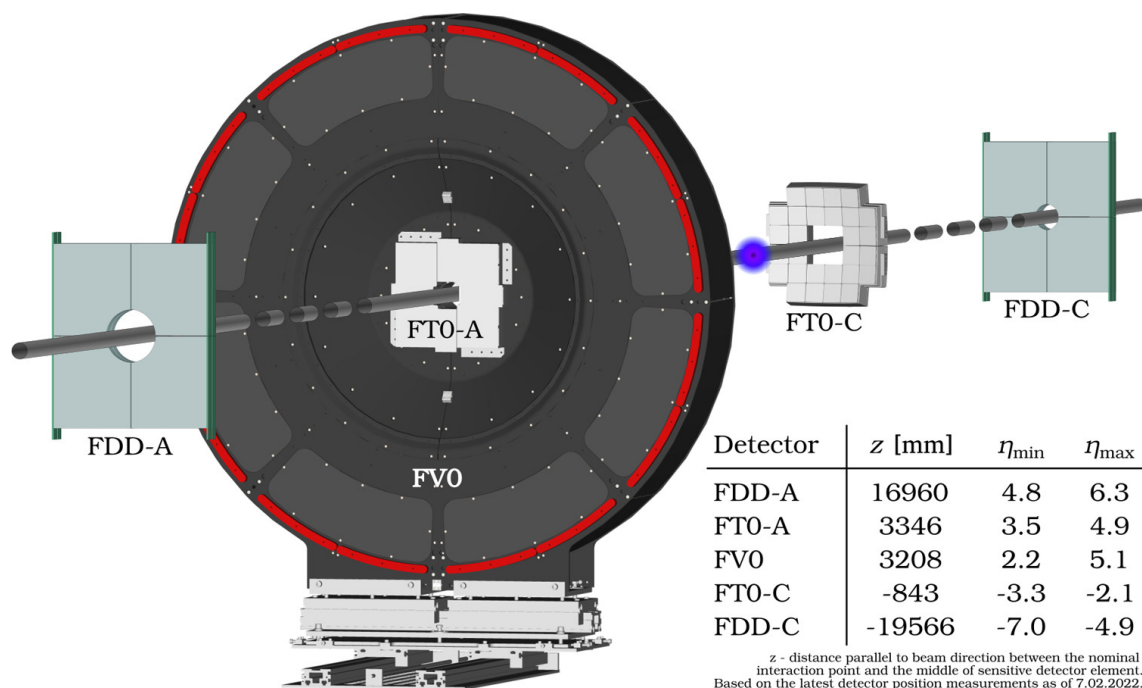


**Figure 4.5:** Layout of the FIT subdetectors. The attached table shows their distance from the nominal IP ( $z$ ) and their pseudorapidity ( $\eta$ ) coverage. Taken from Ref. [30].

on retractable platforms, which allow them to be removed from such a harsh environment when not in active use.

Their upgrade for Runs 3 and 4 involved improvements to control electronics, installation of additional power supplies for photomultiplier voltage dividers, and an update to the readout system.

## MFT

Located between the interaction point and the front absorber of the muon spectrometer (see Fig. 4.6), the Muon Forward Tracker is a newly installed detector designed to greatly augment the capabilities of the spectrometer. It increases muon pointing resolution by matching tracks reconstructed on both sides of the hadron absorber. This allows for the subtraction of multiple scattering of particles within the absorber. It consists of five coaxial discs with detecting elements mounted on both of their faces, carrying a total of 936 ALPIDE silicon sensors, each with a matrix of  $1024 \times 512$  pixels. The detector is capable of tracking of particles with a pseudorapidity range of  $-3.6 < \eta < -2.45$ .

### 4.3.2 Continuous readout mode and the $O^2$ analysis framework

Following its restart after the LS2, the LHC is expected to deliver Pb–Pb collisions at  $\sqrt{s_{NN}} = 5.5$  TeV at an interaction rate of 50 kHz. The resulting integrated luminosity represents a tenfold increase in the data sample of rare triggers, and up to a hundredfold for minimum-bias data. The goal is for the ALICE detector to record a total of  $13 \text{ nb}^{-1}$  of heavy-ion collisions over Run 3 and 4. To accommodate such ambitious plans, several of the subdetectors were upgraded (as covered in the previous section). The main physics

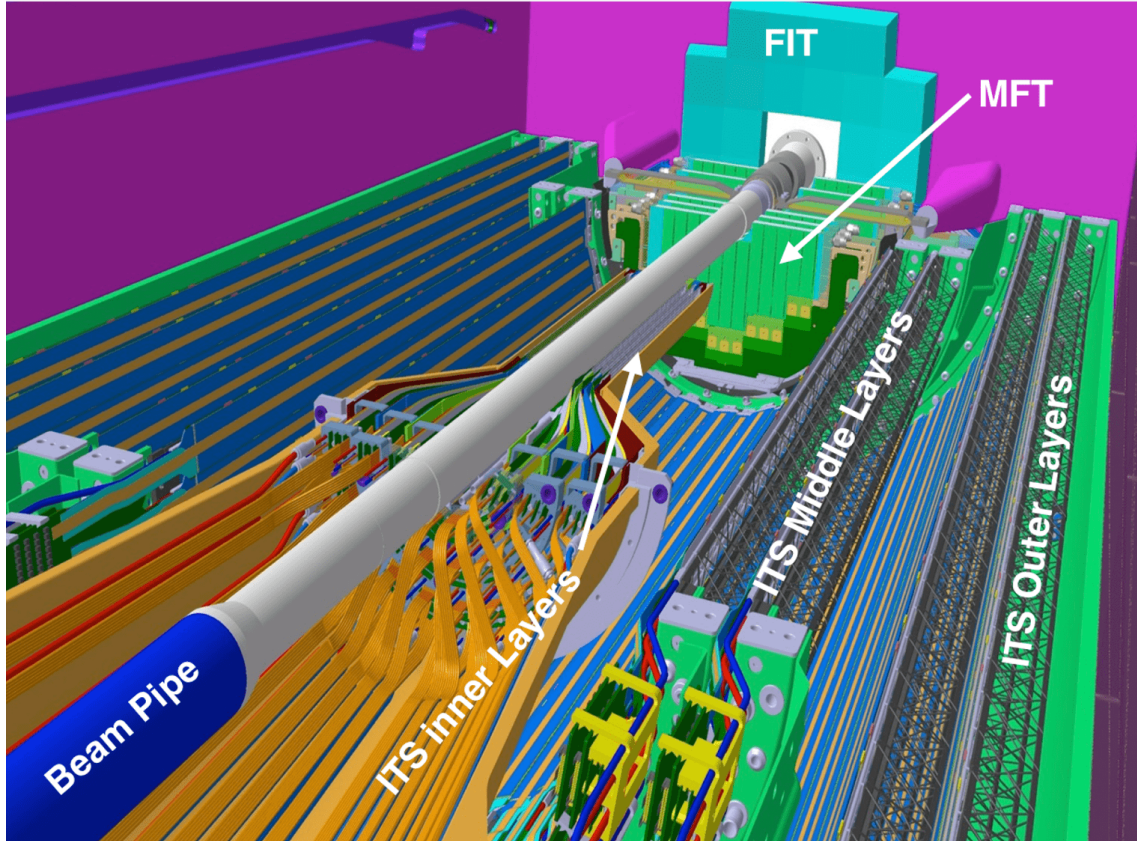


**Figure 4.6:** Diagram of the innermost central barrel detectors of ALICE showing the positioning of the ITS, MFT and FT0-C (FIT). Taken from Ref. [27].

interest for Run 3 is the study of rare probes and hadronisation processes. A characteristic of the majority of the anticipated analyses is a small signal-to-background ratio. It will therefore not be possible to use triggering for event selection, and all collision data will be recorded [32]. The new data-taking paradigm will lead to a detector output of approximately 3.5 TB of raw data per second. This negates the possibility of utilising the same data processing strategy as during Runs 1 and 2 and the experiment will instead rely on the newly designed Online–Offline ( $O^2$ ) software framework and its adjacent computing facility [33].

### Data processing

$O^2$  data processing occurs in two distinct phases, synchronous and asynchronous. The entirety of the data flow is depicted in Fig. 4.7 and will be briefly introduced in the following text.

The primary synchronous stage occurs concurrently with data acquisition and is handled by the  $O^2$  facility, which is located at the ALICE site at LHC Point 2 at CERN. The 3.5 TB/s of raw data are first processed by the First Layer Processing (FLP) nodes. Each FLP handles a portion of a full Time Frame (a fundamental data container), called a sub-Time Frame. The data rate is reduced by a factor of six as approximately 0.6 TB/s reach the Event Processing Nodes (EPNs), which comprise the second layer. The EPNs merge data from the individual FLPs, aggregating full Time Frames in the process. After reconstruction, calibration, and compression, the resulting Compressed Time Frames

(CTFs) are stored in a 60 PB buffer at a rate of 0.1 TB/s. Thus, synchronous processing leads to a total data reduction factor of 35.

Up to several weeks after the initial data processing, the asynchronous phase takes place on the O<sup>2</sup> farm and other Grid nodes, depending on current availability. During this stage, refined calibrations and several following reconstruction steps are performed, after which the final output Analysis Object Data (AOD) files are written to permanent storage and purveyed for analysis.

The processing flow will be nearly identical for data from pp collisions, although in this case, the expected data rates require further filtering through the implementation of physics-oriented triggers. pp data CTFs will therefore not contain information from all collisions, as only events of interest will pass through the trigger filters applied during the asynchronous stage [33].

## **O<sup>2</sup> analysis framework**

The O<sup>2</sup> framework is built upon three layers. The Transport Layer builds the software topology and prepares the data for transport through the network in the form of FairMQ messages. Next, the Data Model provides computer-language-independent descriptions of these messages and optimises their data formats. Finally, the Data Processing Layer provides the mediation between the user's task and the message exchange mechanism [33].

The analysis input AO(2)D data are organised into flat tables. This data structure allows for a high degree of I/O cost optimisation and parallelisation. The tables are modular and may be joined, filtered, and partitioned. To comply with the data reduction requirements, they do not store dynamic values, which are in turn computed on demand. The standard output of an analysis task is a ROOT file.

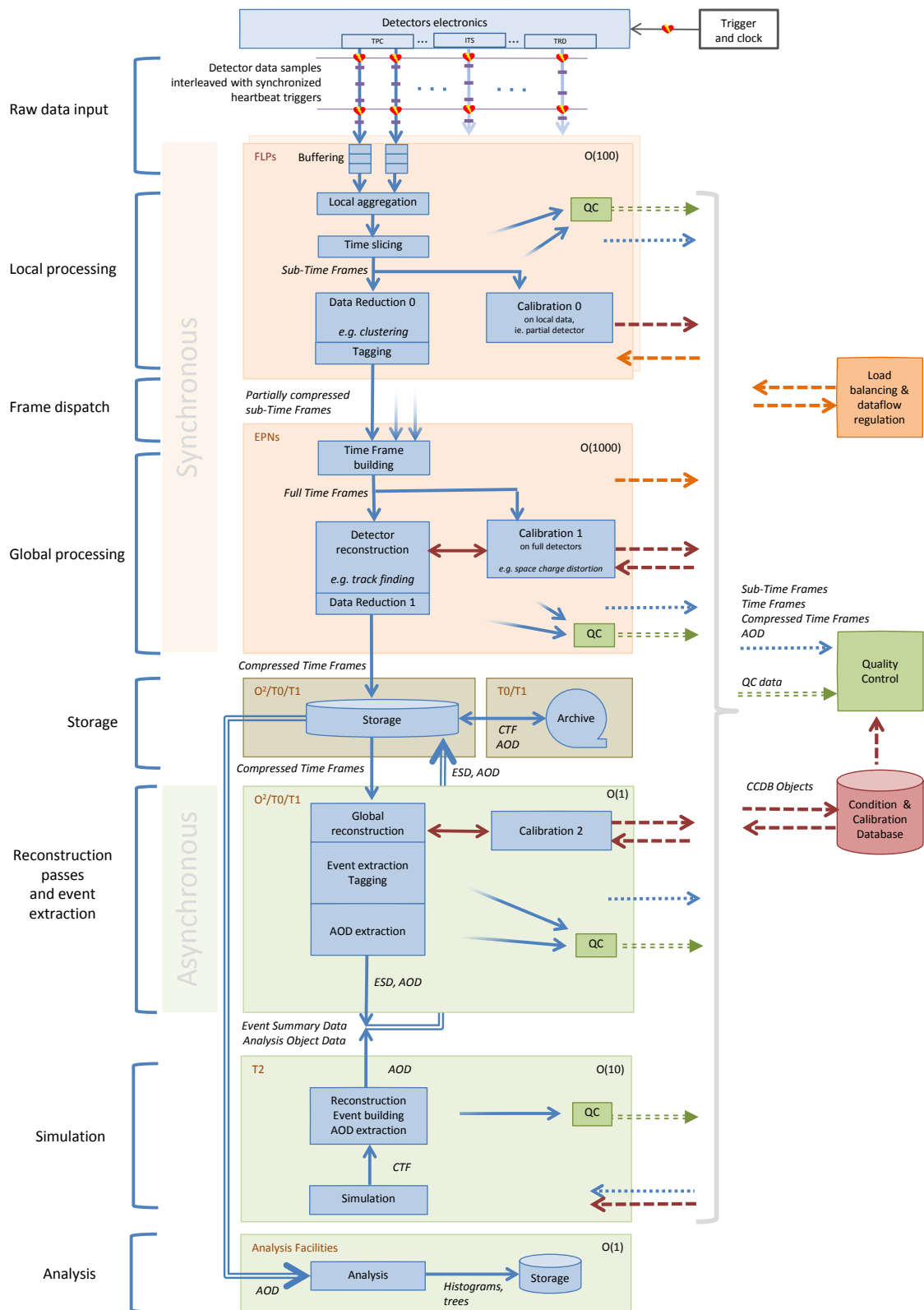


Figure 4.7: Data processing flow of the O<sup>2</sup> system. Taken from Ref. [32].

# Chapter 5

## Previous ALICE measurements of coherent photoproduction of $\rho^0$

The ALICE Collaboration performed several studies of photoproduction using data collected during Run 2. Of particular interest is the  $\rho^0$  meson, as it is the most copiously photoproduced vector meson (see Fig. 3.4). The experimental set-up, analysis procedure, and results of two measurements performed by the Collaboration utilising data gathered from Pb–Pb collisions at  $\sqrt{s_{\text{NN}}} = 5.02$  TeV and Xe–Xe collisions at  $\sqrt{s_{\text{NN}}} = 5.44$  TeV (as described in Refs. [34] and [35], respectively) will be summarised in this chapter.

### 5.1 $\rho^0$ photoproduction in Pb–Pb UPCs at $\sqrt{s_{\text{NN}}} = 5.02$ TeV

This measurement of  $\rho^0$  photoproduction in Pb–Pb ultra-peripheral collisions was performed on data collected during the 2015 heavy-ion run. As mentioned previously, the photon flux grows with  $Z^2$ , which leads to particularly intense fluxes for lead ions. In consequence, secondary photon exchanges between the incident ions (independent of photoproduction) cause electromagnetic excitations, producing neutrons at beam rapidities. This allows for the separation of events into nuclear breakup classes according to the number of neutrons observed in the event: 0n0n (no neutrons on either side), 0nXn or Xn0n (neutrons observed on one side), and XnXn (neutrons on both sides of the IP).

#### 5.1.1 Experimental set-up

The  $\rho^0$  was reconstructed from its decay into a  $\pi^+\pi^-$  pair, whose tracks were measured by the ITS (with its SPD layers also participating in triggering) and the TPC. The V0 and AD detectors served as triggers. Finally, the ZDCs were used for the detection of beam-rapidity neutrons. Their energy resolution allows for the separation of events with zero or a few neutrons, distinguishing between the 0n and Xn breakups.

The complete event trigger had two main components. The SPD (two innermost layers of the ITS) provided a topological trigger, selecting events with two tracks whose azimuthal angle separation was greater than 153 degrees. As coherently produced  $\rho^0$  have small  $p_{\text{T}}$ , they decay into pions produced nearly 'back-to-back' in their azimuth. Both arms of the AD and V0 detectors were used as vetoes, rejecting events with hadronic interactions. The integrated luminosity of the measurement was  $(485 \pm 24)$   $\text{mb}^{-1}$ .

## 5.1.2 Analysis procedure

### Event selection

In addition to meeting the trigger criteria, events were considered for further analysis only if they contained precisely two tracks with opposite electric charge. Both tracks were required to have at least 50 space points in the TPC and hits in both layers of the SPD. The limit of their DCA (distance of closest approach) to the event vertex was set to 2 cm in the longitudinal direction (along the  $z$  axis) and  $0.0182 + 0.0350/(p_{\text{T}}^{\text{trk}})^{1.01}$  cm in the transverse plane (where  $p_{\text{T}}^{\text{trk}}$  denotes the transverse momentum of the track).

The energy lost by the tracks on passing the TPC was used for PID purposes. Measured in units of the standard deviation  $\sigma_{\pi}$  from the value expected from the Bethe formula, the track pair was accepted if  $(n\sigma_{\pi^+})^2 + (n\sigma_{\pi^-})^2 < 5^2$ . For subsequent computations, both tracks were assumed to be pions.

Furthermore, the rapidity, transverse momentum, and mass of the track pairs were required to be within the intervals of  $|y| < 0.8$ ,  $p_{\text{T}} < 0.2$  GeV/ $c$ , and  $0.55 < m < 1.4$  GeV/ $c^2$ , respectively. The limits on  $p_{\text{T}}$  and  $m$  were chosen as such to filter out background from the photoproduction and subsequent decay of the  $\omega$  vector meson ( $\omega \rightarrow \pi^+\pi^-\pi^0$ ). These events leave signals mainly in lower masses and higher transverse momenta, and are therefore suppressed in the final sample following the presented event selection. Moreover, the lower limit of the pair invariant mass compensates for the inability to distinguish electrons from pions at very low track momenta [36]. The requirement imposed on the final state transverse momentum also limits the contribution from incoherent photoproduction.

The vetoes from the AD and V0 detectors were reapplied during offline reconstruction, as it is more precise than online information. Any signal in either of the ADA/C and V0A/C detectors within the time window corresponding to beam–beam interactions caused a rejection of the event.

In total, almost 57 thousand events passed the selection criteria, their invariant mass and transverse momentum distributions are plotted in Fig. 5.1. Based on activity within the ZNA/C detectors, they were further subdivided into the aforementioned breakup classes.

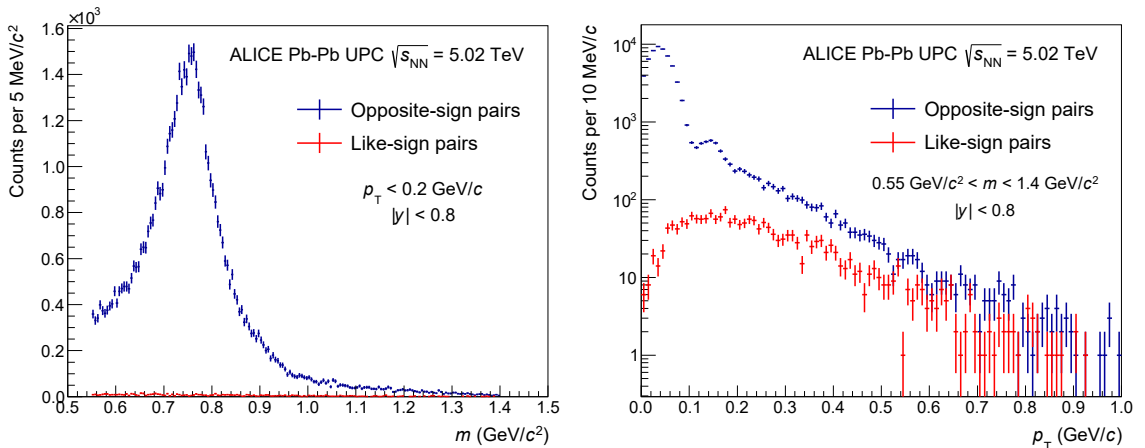


**Figure 5.1:** Invariant mass and transverse momentum distributions for track pairs passing the selection criteria. Adapted from Ref. [34].

## Background and experimental effects corrections, signal extraction

For the estimation of the shape and amount of any background from events with other charged tracks outside the detector acceptance, the distributions of like-sign pairs otherwise fulfilling the same selection criteria were studied. They are plotted in Fig. 5.1 alongside the opposite-sign pairs and were subtracted from the signal sample. Other sources of background include the already mentioned decay of the  $\omega$  meson, incoherent interactions, and two-photon processes ( $\gamma\gamma \rightarrow \mu^+\mu^-$ ).

A number of other experimental effects, including detector inefficiencies, are discussed in more detail in the source article (Ref. [34]) and appropriately accounted for in the analysis. Of note is the substantial loss of signal due to vetoes upon the detection of other particles created in nuclear dissociations. This amounts to the loss of  $(26 \pm 4)\%$  of  $0nXn$  events and  $(43 \pm 5)\%$  of  $XnXn$  events.

Acceptance times efficiency ( $A \times E$ ) corrections evaluate the effects of detector properties and the analysis procedure on obtainable data. They were determined from two Monte Carlo (MC) event samples generated with the STARlight program simulating a purely coherent photoproduction (with a Breit-Wigner distribution) and following a flat-mass distribution, respectively. The samples were passed through a simulation of the ALICE apparatus and subjected to the analysis workflow. The invariant mass histograms of reconstructed events passing the selection criteria were subsequently divided by the histograms of generated events. The obtained values are shown in Fig. 5.2 and result in similar corrections from both approaches. As the number of events generated around the expected  $\rho^0$  invariant mass peak is larger in the sample following a Breit-Wigner distribution, the obtained  $A \times E$  values are affected by smaller statistical uncertainties in comparison with the second sample. The purely coherent sample also suffers from greater bin migration effects (events spreading to neighbouring bins as a result of limited reconstruction resolution). This effect was also expected from real data and the purely coherent sample was therefore deemed to better align with real reconstruction effects [36].

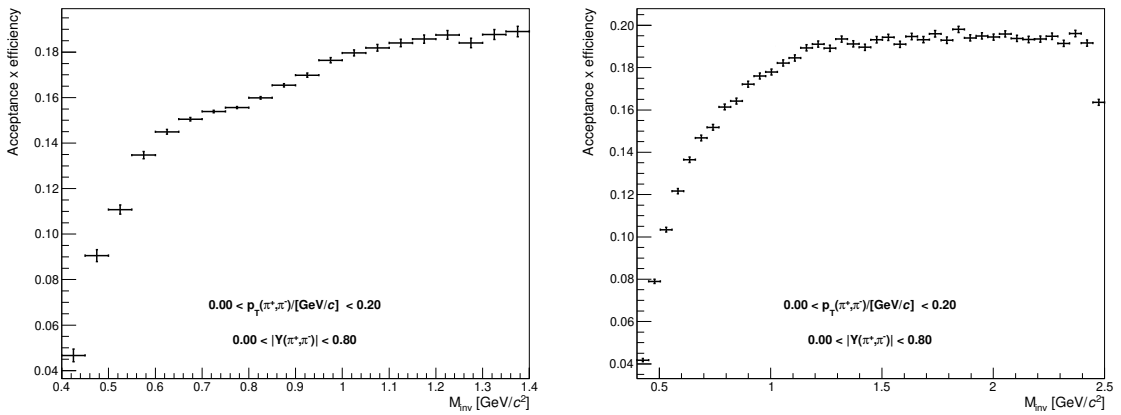


**Figure 5.2:**  $A \times E$  values obtained from a STARlight MC sample produced using a Breit-Wigner distribution (left) and flat-mass distribution (right). Adapted from Ref. [36].

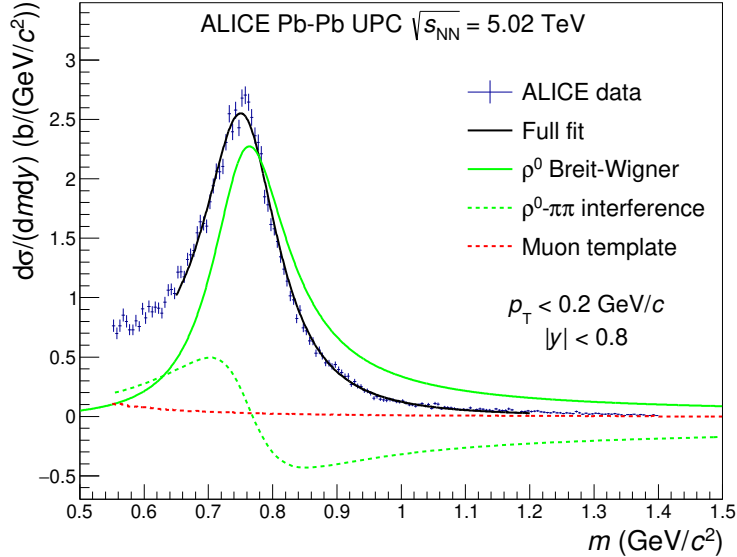


**Figure 5.3:** Fitted invariant mass distribution of the photoproduced  $\rho^0$  mesons. Also displayed are the individual components of the fit. Taken from Ref. [34].

The corrected invariant mass distribution was fitted with a Söding formula shifted by a linear term  $M$  accounting for the contribution of 2-photon processes

$$\frac{d^2\sigma}{dm dy} = |A \cdot BW_\rho + B|^2 + M, \quad (5.1)$$

where  $BW_\rho$  is the Breit-Wigner function describing the  $\rho^0$  distribution normalised by the  $A$  factor and  $B$  accounts for the non-resonant amplitude. The result of this fit can be seen in Fig. 5.3. The obtained values of  $m_{\rho^0} = 769.5 \pm 1.2$  (stat.)  $\pm 2.0$  (syst.) MeV/ $c^2$  and  $\Gamma(m_{\rho^0}) = 156 \pm 2$  (stat.)  $\pm 3$  (syst.) MeV/ $c^2$  are both consistent with their corresponding PDG counterparts. The estimation of systematic uncertainties is discussed in great detail in the source reference.

### 5.1.3 Results

The cross section for the coherent photoproduction of  $\rho^0$  was obtained by integrating the Breit-Wigner function over the invariant mass range from  $2m_\pi$  to  $m_{\rho^0} + 5\Gamma(m_{\rho^0})$ . The measurements were performed in three intervals of absolute value of rapidity and are shown in Fig. 5.4 for the different nuclear breakup classes in comparison with the predictions of several photoproduction models.

The already introduced STARlight model does not take into account the elastic part of the vector meson–nucleon cross section and underestimates the experimental results in the majority of cases (at approximately a  $2\sigma$  difference). The GKZ model is based on a modified vector-dominance model and incorporates the effects of nuclear shadowing. Out of the compared models, it presents the overall best agreement with the results. The GMMNS and CCKT models arise from two different approaches to the colour-dipole model. Accounting for the uncertainties, the agreement between the measurement and the models is generally satisfactory.



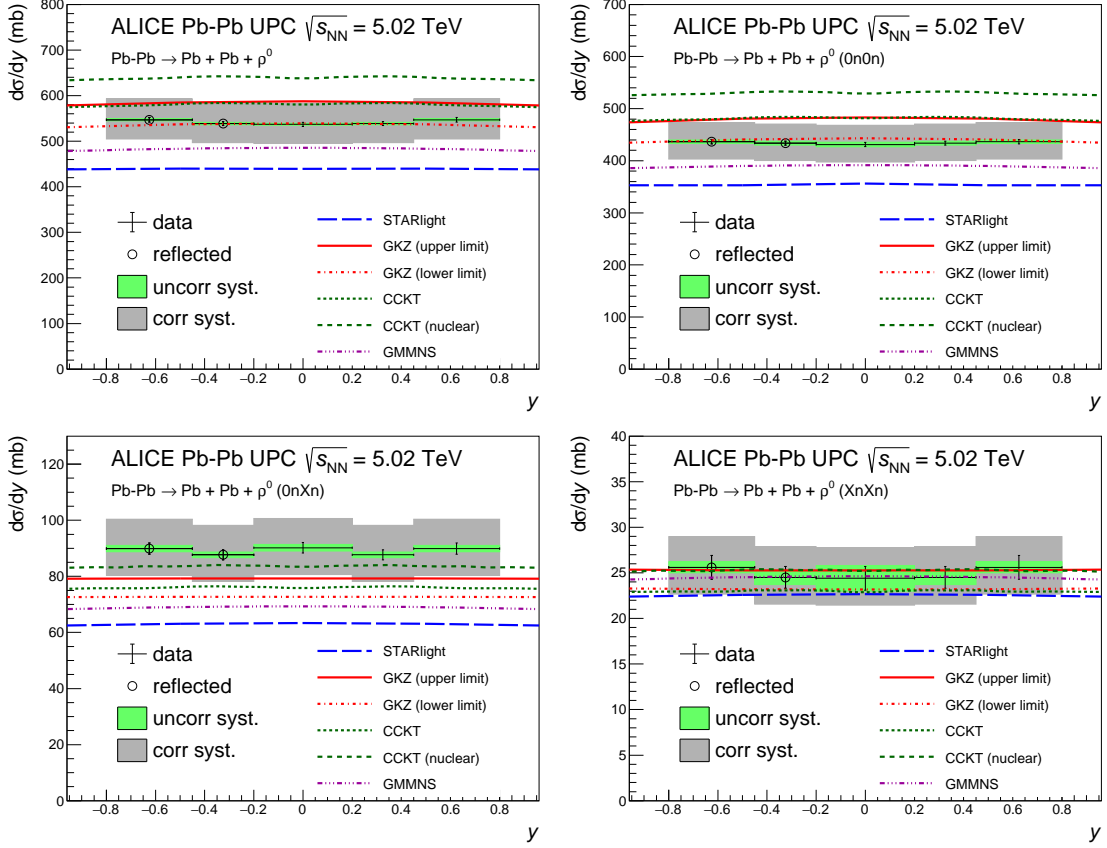


**Figure 5.4:** Cross sections of coherent photoproduction of  $\rho^0$  mesons in Pb-Pb UPCs as a function of rapidity. Displayed are the cross sections for no forward-neutron selection and for the three nuclear breakup classes. The results are compared with the predictions of several theoretical models. Taken from Ref. [34].

## 5.2 $\rho^0$ photoproduction in Xe–Xe UPCs at $\sqrt{s_{\text{NN}}} = 5.44$ TeV

Collisions of Xe ions in the LHC provided the ALICE Collaboration with a unique opportunity to study photoproduction with a new ion species. Combined with the previous results from Pb–Pb collisions, it is possible to study the nucleon number ( $A$ ) dependence of photoproduction, the effects of nuclear shadowing on this process, and the black-disc limit of QCD. The production of neutrons at beam rapidities is substantially suppressed in comparison with the lead-ion collisions, as the photon fluxes around the lighter xenon ions are much weaker.

### 5.2.1 Experimental set-up

Similarly to the measurement described in the previous section, the decay products of the  $\rho^0$  meson were measured using the ITS and TPC detectors, and the beam-rapidity neutrons were detected in the ZDCs.

The event trigger required signal in both SPD layers as well as the pads of the TOF detector. For vetoing, only the V0 was used. The integrated luminosity used in the analysis was  $(279.5 \pm 29.9) \text{ mb}^{-1}$ .

### 5.2.2 Analysis procedure

#### Event selection

Satisfying the event trigger, the tracks were required to meet several other criteria to be selected for the analysis. Both tracks of opposite sign were required to originate no further than 10 cm from the primary vertex (in the  $z$  direction) and be fully in the pseudorapidity range covered by the detector ( $|\eta| < 0.8$ ). Again, they had to produce a signal in both layers of the SPD and have at minimum 50 space points in the TPC. The pion PID selection was kept the same as for the Pb–Pb measurement. Finally, the transverse momentum of the pion pair had to be below 0.15 GeV/ $c$ .

In total, 1827 events passed the presented selection. Their mass and transverse momentum distributions are plotted in Fig. 5.5.

#### Signal extraction

To estimate systematic errors, the signal extraction was repeated many times with varying fit parameters. Several other corrections were performed, as described in detail in Ref. [35].

In contrast with the Pb–Pb UPCs, fewer events (estimated at  $(1.7 \pm 0.2)\%$ ) were lost from false V0 vetoes caused by additional charged particles passing the detector. The substantial decrease was primarily caused by the lower intensity of the photon fluxes and the absence of AD vetoing.

The acceptance times efficiency corrections were again determined from a sample of MC events generated with STARlight, the results are depicted in Fig. 5.6. The noticeable decrease compared with the Pb–Pb analysis  $A \times E$  values (Fig. 5.2) was caused by the rather stringent requirement for pion track hits in the TOF detector.

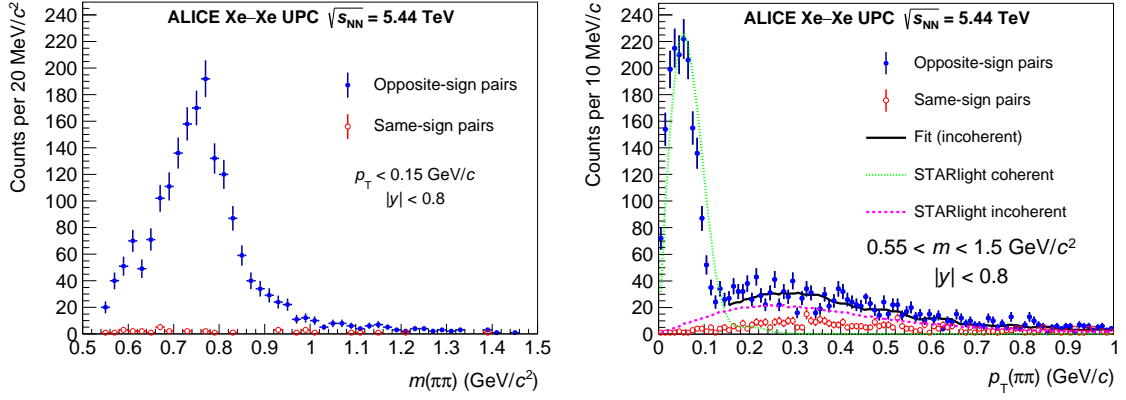


**Figure 5.5:** Uncorrected invariant mass and transverse momentum distributions of eligible opposite- and same-sign pion track pairs. The  $p_T$  distribution also shows the templates for coherent and incoherent production obtained from STARlight (MC events) and an example fit to the incoherent contribution. Taken from Ref. [35].

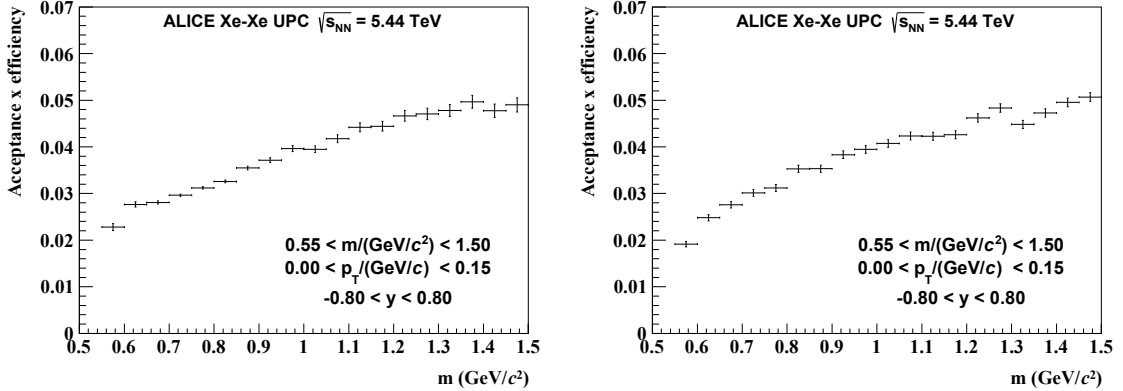


**Figure 5.6:** A×E values obtained from a STARlight MC sample produced using a Breit-Wigner distribution (left) and flat-mass distribution (right). Adapted from Ref. [36].

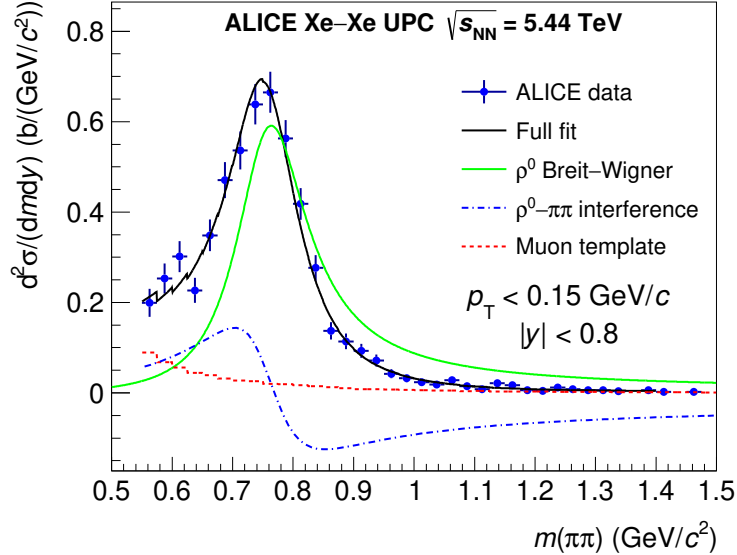


**Figure 5.7:** Fitted invariant mass distribution of selected pion pairs. Also displayed are the individual components of the fit. Taken from Ref. [35].

The corrected mass distribution was fitted in a manner identical to the Pb–Pb UPCs analysis, with the result depicted in Fig. 5.7.

### 5.2.3 Results

The coherent  $\rho^0$  photoproduction cross section was measured at midrapidity and again compared with the STARlight, GKZ, GMMNS, and CCKT models, as shown in Fig. 5.8. As can be seen, all models overestimate the data by more than  $1\sigma$  (with the upper limit of GMMNS exceeding  $3\sigma$ ). For comparison, the events were divided into the nuclear breakup classes presented in the analysis of Pb–Pb UPCs. As expected, only about 10% of events were accompanied by beam-rapidity neutrons (with only approximately 1% of the events belonging to the XnXn class).

The midrapidity cross section measurements from both presented analyses were converted into  $\sigma_{\gamma A}$  by dividing  $\sigma_{AA}$  (gained by integration of the measured  $d\sigma_{AA}/dy$ ) by two times the corresponding total photon fluxes (stemming from Eq. (3.6)). Although they differ slightly, the midrapidity photon–nucleus centre-of-mass energies per nucleon of the two measurements were taken as  $W_{\gamma A, n} = (m_\rho \sqrt{s_{NN}})^{1/2} \approx 65$  GeV, and the corresponding photonuclear cross sections plotted in Fig. 5.9 as a function of  $A$ .

The obtained values (together with a result from another measurement from H1) were fitted by a power-law model  $\sigma_{\gamma A}(A) = \sigma_0 A^\alpha$ . A  $\chi^2/\text{dof} = 1.48$  fit yielded parameters of  $\sigma_0 = (0.0117 \pm 0.0009)$  mb and  $\alpha = 0.963 \pm 0.019$ . A fully coherent cross section should scale with  $\alpha = 4/3$ , which is far from the observed slope. This suggests a significant suppression of the photoproduction process from nuclear shadowing effects. Conversely, the values are considerably higher than what would be expected from the black-disc limit (scaling with the geometric area of the nucleus as  $\alpha = 2/3$ ). It should be noted that the closeness to the incoherent slope is purely coincidental and does not imply incoherent behaviour. Predictions from the CCKT and GKZ models are in good agreement with the data.

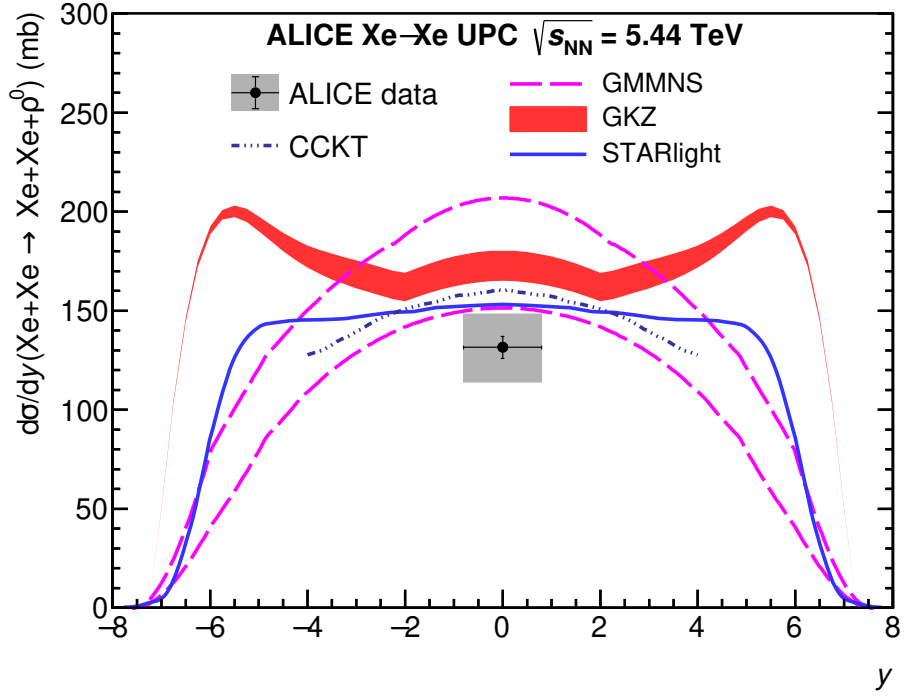


**Figure 5.8:** Measured cross section of coherent photoproduction of  $\rho^0$  in Xe-Xe UPCs in comparison with theoretical predictions. Taken from Ref. [35].

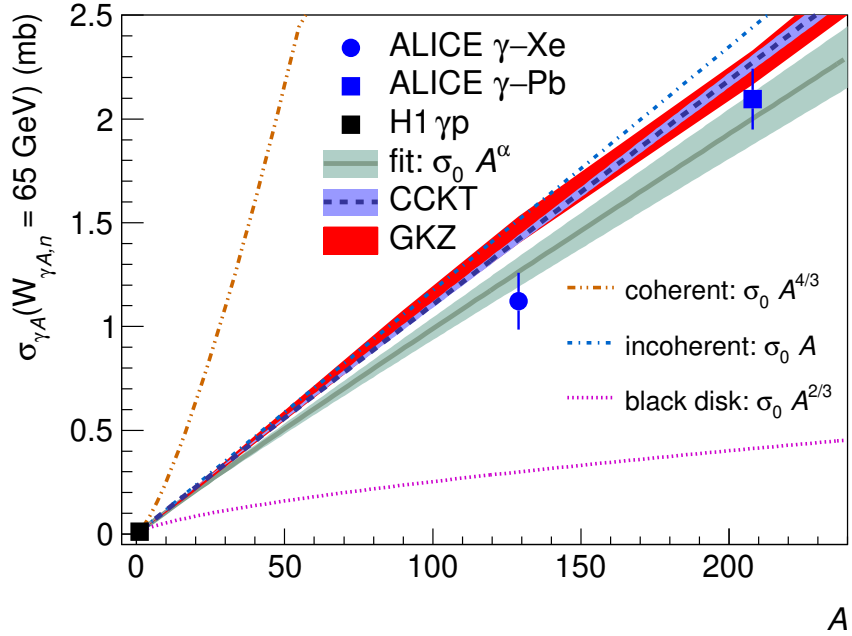


**Figure 5.9:**  $A$ -dependence of  $\sigma_{\gamma A}$  for coherent  $\rho^0$  production. Also depicted is its power-law fit as well as the expectations from three extreme cases (coherent, incoherent, and black-disc limits), and two theoretical models (CCKT and GKZ). Taken from Ref. [35].

# Chapter 6

## Analysis of simulated data

As the O–O run currently scheduled for 2024 will be the first time the LHC will have actuated collisions of oxygen beams, no real data presently exists for this specific collision system. The preliminary analysis performed in this thesis is to serve a preparatory function, with a goal of setting up the analysis framework to facilitate and accelerate further progress once the data become available. For this purpose, a small sample of O–O MC events has been generated with STARlight. The program itself, the generated dataset, and the preformed analysis (namely the calculation of acceptance times efficiency correction factors) will be introduced in this chapter.

Since the amount of available O–O MC data is rather limited, studies were also performed on simulated Pb–Pb events from a newer and more extensive dataset. This will be briefly introduced in Sec. 6.3.

### 6.1 STARlight MC generator

STARlight (as described in Ref. [12]) is a Monte Carlo generator used extensively for the studies of UPCs and associated interactions. It implements the theoretical model described in Sec. 3.2.1 in order to calculate cross sections, generate MC events, and simulate any decays in the concerned processes. The program is capable of simulating both two-photon and photonuclear interactions (the latter of which may also be treated as the coherent or incoherent case). In addition, it is able to take into account the additional photon-induced events leading to beam-rapidity neutron emission.

Many parameters (see the source Ref. [12] for the full list) may be specified by the user in an input file used for the subsequent execution of the program. This includes beam properties such as  $Z$ ,  $A$ , and the beam energy (specified through the beam Lorentz factor calculable through Eq. (3.4)). All parameters may be set individually, which allows for the study of numerous combinations of collision parameters. It should be noted however that STARlight has been optimised for simulations of collisions observable in current accelerators (namely the LHC and RHIC) and deviations from similar parameter values may cause inaccuracies.

The cross section calculations are based on parametrizations of data collected by HERA from  $\gamma p \rightarrow V p$  events. For the necessary computations, the program follows a Glauber calculation, assuming either narrow or wider resonances (described by the Breit-Wigner

distribution). This can also be specified by the user (`PROD_MODE` parameter), but influences only the cross section calculation, not the subsequent generation of MC events (which is always done following the Breit-Wigner function). Furthermore, the transverse momentum spectra may be generated assuming independent photoproduction on the two nuclei, or including interference between the two contributions (the strength of which may also be changed). The assumed nuclear breakup modes can be influenced through the `BREAKUP_MODE` setting.

The execution of STARlight happens in two distinct phases. The calculation of cross sections and other kinematic variable distributions is performed in the first phase. The results are stored in look-up tables, which are then used in the second phase, where MC events are generated. Whilst it was initially intended to work as a standalone program, the generator has been interfaced into the  $O^2$  framework. Thus, it is able to conveniently provide the standard AO2D file as output, streamlining further analyses.

## 6.2 O–O dataset

For the study of  $\rho^0$  photoproduction in O–O collisions, a 2500-event sample was generated with STARlight using the parameters summarised in Tab. A.1 found in Appendix A. The simulation was executed locally, since the ALICE framework has not been prepared for this task until rather recently. This was also the main limiting factor for the obtainable sample size. The input file was set to generate collisions of  $^{16}\text{O}$  ions and simulate coherent photoproduction of  $\rho^0$ s and their subsequent decay into a charged pion pair. The sample was generated without interference and no requirement on ion breakup was imposed. The pseudorapidity coverage of the decay products was set to  $-4.0 < \eta < 1.5$  in order to cover the entire acceptance of the ALICE detector. This allows for the study of several event geometries: central, semi-forward, and forward; although this work will be focused only on the central topology. No restriction on the pion transverse momenta was imposed.

The properties of all particles in the generated MC dataset are known without ambiguity. To simulate real data, the events were passed through a GEANT 4 simulation of the ALICE detector, which introduces commonly observed effects seen in measured data, such as reconstruction inefficiencies, collision association ambiguities, etc. Thus, the data may be studied at the generator or reconstruction level. Both approaches will be utilised in the subsequent analysis for the calculation of  $A \times E$  correction factors.

### 6.2.1 Generator-level data

Generator-level data are obtainable by accessing the MC information stored within the AO2D file. Both the  $\rho^0$  mesons and the decay  $\pi^\pm$  tracks may be studied in this manner.

Spectra of select variables ( $m$ ,  $p_T$ , and  $y$ ) describing the generated  $\rho^0$  mesons are plotted in Fig. 6.1. The vector meson masses are simulated assuming a Breit-Wigner distribution. Transverse momenta of the  $\rho^0$ s are inherently limited by the coherence requirement, and consequently reach only relatively low values. As photoproduction is a diffractive process, several diffraction peaks should be present in this distribution. This is however not apparent due to the limited size of the dataset (note that this is slightly clearer in the spectrum from the lead data). Since the main contributors to higher- $p_T$   $\rho^0$ s are incoherent

processes, only the first peak is desirable for coherent photoproduction studies and as such is generally isolated from the subsequent peaks by applying appropriate selection criteria.

The transverse momentum, azimuthal angle ( $\phi$ ), and rapidity distributions of the pion tracks resulting from the decay of the vector mesons are plotted in Fig. 6.2. As the coherently photoproduced  $\rho^0$ s have low  $p_T$ , the pions are expected to be produced with an angular separation of almost  $\Delta\phi \approx \pi$  (following momentum conservation). This is apparent from the pion  $\phi$  plot in the form of two linear structures.

## 6.2.2 Reconstructed data selection

Reconstructed data are gained by the simulation of detector effects on the MC dataset. They are stored in the same AO2D file and may be accessed either in an isolated manner (and treated as real data), or in conjunction with the MC information.

Standard analysis procedures, such as those described in Chapter 5, involve several steps to filter out background and select desirable tracks for the reconstruction of the photoproduced vector mesons. Although the presented analysis was perhaps not as thorough and extensive, it generally followed a similar strategy.

For further consideration, the tracks were required to have opposite electric charge and pass a PID criterion based on the particle identification capabilities of the TPC detector. Tracks passed only when their pion-hypothesis  $n\sigma$  values fell within  $|n\sigma_\pi| < 5$ . Following this, for further calculations they were presumed to be pions with a mass of  $0.139570 \text{ GeV}/c^2$  (as per Ref. [37]). It should be noted that one may also employ TOF PID, but as will be shown further, most of the reconstructed tracks did not reach the TOF detector, and therefore do not have this information available.

Most analyses impose further requirements for track selection. This is however not the case in the analysis for this thesis. With the new upgrades to the ALICE detector and the switch to the  $O^2$  framework, it is not yet certain what exactly constitutes a 'good' track. Further studies into this problematic must be performed. Nonetheless, select extracted detector information is included in Fig. 6.3 for illustrative purposes. The data are gathered from tracks which passed the PID restriction, but otherwise no selection was applied to them (their charge was also not distinguished). Examined were the total number of hits and the track  $\chi^2$  within the ITS, TPC, and TOF detectors, the number of found clusters in the ITS and TPC, and the number of crossed rows of the TPC.

In the final step of the procedure, the particles reconstructed from the preselected pion tracks were required to further satisfy the following:  $|y| < 0.8$ ,  $p_T < 0.17 \text{ GeV}/c$ , and  $0.6 \text{ GeV}/c^2 < m < 1.2 \text{ GeV}/c^2$ . The rapidity requirement selects only centrally produced mesons. The transverse momentum and invariant mass selections generally serve to filter out background and other unwanted contributions to the signal. As stated previously in Sec. 5.1.2, for  $\rho^0$  analyses, similar criteria are used to exclude the contribution from  $\omega$  meson decays, which present with similar experimental signature as the decaying  $\rho^0$ s. Furthermore, the  $p_T$  selection discards incoherent processes. Neither of these two concerns are particularly relevant for the studied dataset, as the only process considered in the simulation was coherent  $\rho^0$  production. However, a certain amount of filtering was necessary, as an examination of the reconstructed data revealed the presence of charged tracks with low values of  $p_T$ ,  $m$ , and  $y$ , which greatly interfered with the reconstruction. These are presumed to be electrons and positrons created in  $\gamma\gamma \rightarrow e^+e^-$  events added into the simulation. While PID did remove some of this contamination, sufficient clarity



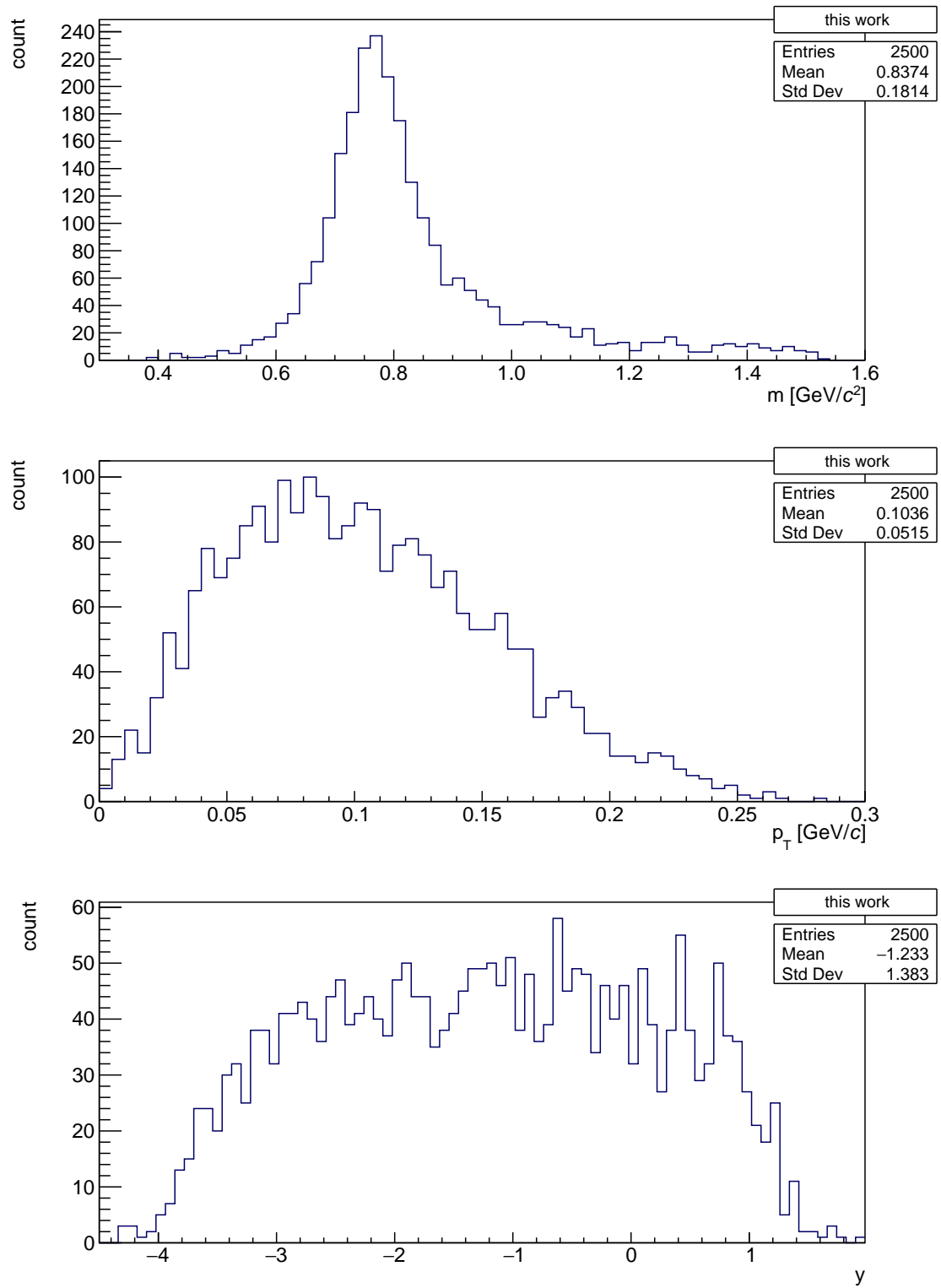


**Figure 6.1:** Generator-level invariant mass, transverse momentum, and rapidity distributions of generated  $\rho^0$  mesons from O-O events.

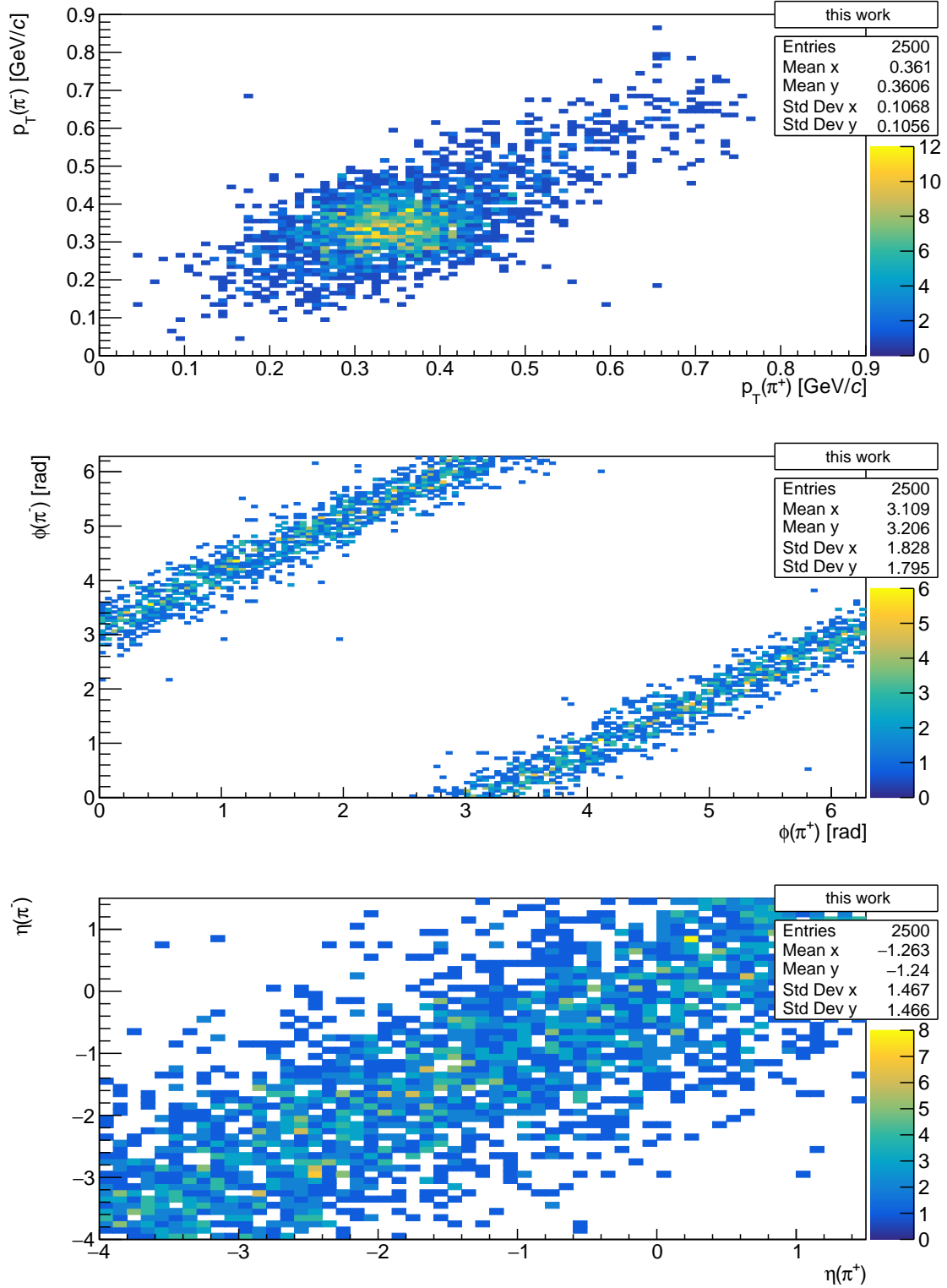


**Figure 6.2:** Transverse momentum, azimuthal angle, and rapidity distributions of generated pion tracks from O–O events.

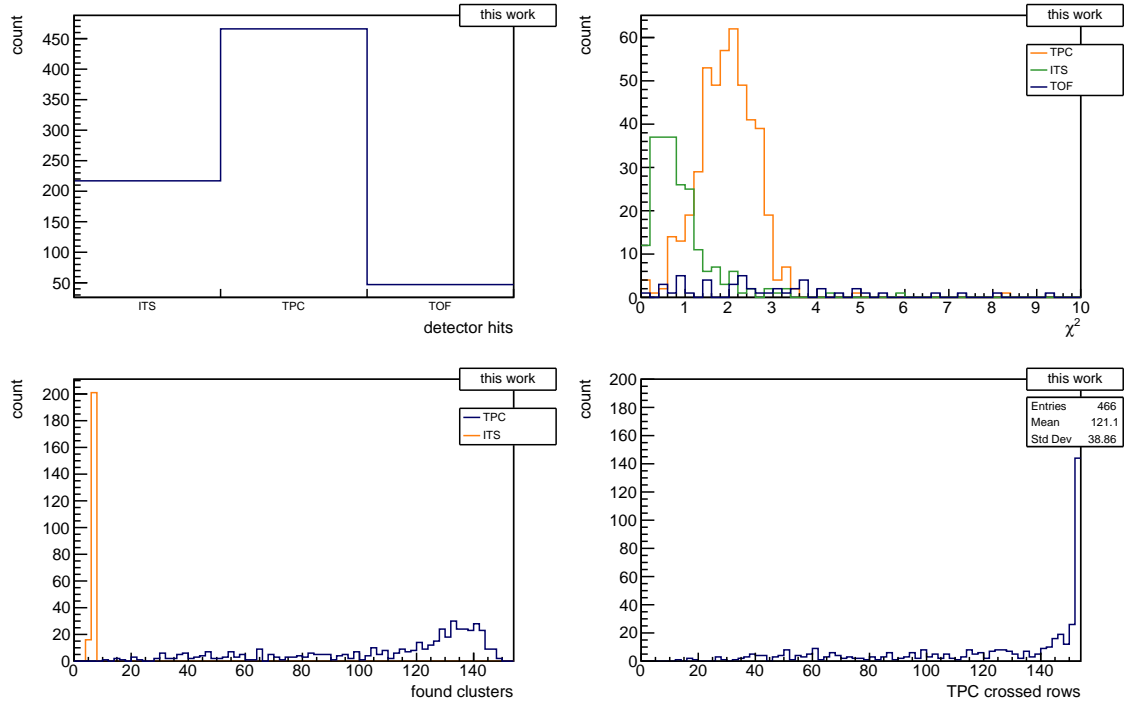


**Figure 6.3:** Select track selection properties of O–O data reconstructed tracks passing the PID requirement. Shown are the total number of detector hits, the track  $\chi^2$  in the individual detectors, the number of found clusters within the ITS and TPC detectors, and the number of crossed TPC rows.

was achieved only after the application of the reconstructed particle selection criteria.

As the initial data sample included only 2500 produced vector mesons, the dataset obtained following the analysis procedure suffers from a very low number of events. Out of the 858 centrally produced (i.e. with  $|y| < 0.8$ )  $\rho^0$ s, only 73 events fulfilling the described selections were reconstructed. Their invariant mass, transverse momentum, and rapidity spectra will be presented alongside the calculated  $A \times E$  factors in the following section.

### 6.2.3 $A \times E$ calculation

The concept of acceptance times efficiency corrections has already been touched upon in Chapter 5, since they were utilised in both of the presented measurements. As their computation relies only on MC data, they present an ideal candidate for preliminary analysis of the available dataset.

$A \times E$  is a measure describing the effect of detector properties (acceptance, reconstruction efficiency, etc.) and the analysis procedure itself on data. Its calculation is rather straightforward. An MC sample is run through a detector simulation. This imprints the numerous reconstruction uncertainties, which affect all measurements with the detector. It may be further treated as real data and subjected to the specific analysis workflow used in the study. Only a portion of the input number of events will remain after the procedure. To determine the numerical value of acceptance times efficiency, the number of collected output events is simply divided by the number of input events, which is also precisely

known due to the MC nature of the dataset. This may be written as

$$A \times E = \frac{N_{\text{reconstructed}}(\text{full selection})}{N_{\text{generated}}(\text{rapidity selection})}, \quad (6.1)$$

where the rapidity selection in the denominator ensures that only particles produced in the studied rapidity interval are counted in the generator-level input.

The calculation of statistical uncertainties for the  $A \times E$  values is rather ambiguous, as several differing methods may be utilised to that end. While the events‘ passing (or not) of the selection criteria is a binomial process, the reconstruction has unforeseeable effects on the kinematic distributions. For this reason, there is no obvious choice for an appropriate statistical model. If the reconstruction influence is ignored and the uncertainties treated according to the binomial hypothesis, problems may arise in the event that an  $A \times E$  value of 0 or 1 is reached. In this case, this method would yield zero statistical uncertainty. Although this is theoretically not impossible, the accuracy of such a result is dubious. A frequently employed method is the so-called Clopper-Pearson interval. It is the PDG-recommended manner of efficiency uncertainty calculation and also the default technique used by the ROOT framework [38]. Lastly, this analysis also explored an approach developed by Ullrich and Xu using Bayesian statistics. Their technique was described in Ref. [39], which has since been retracted. Consequently, the results obtained from this method only serve as illustration and will not be considered further.

In practice, the acceptance times efficiency calculation procedure is usually approached as a binwise operation on spectra obtained from the given analysis. In this thesis, it was performed for the invariant mass, transverse momentum, and rapidity distributions gained following the workflow described in the previous section. The results are plotted in Figs. 6.4, 6.5, and 6.6, respectively. For demonstrative purposes, the uncertainties were computed using both of the discussed Clopper-Pearson and (ad hoc called as such) Ullrich-Xu methods. As can be observed, for a sufficiently high number of events, both approaches yield similar values. Systematic uncertainties were neglected in this analysis.

To get a sense of an overall value, the binwise results for all three examined spectra were fitted (considering the Clopper-Pearson uncertainties) by a simple constant function, with the results summarised in Tab. 6.1. It should be noted that this is most definitely a grave oversimplification, as the response functions generally have a much more complicated progression. A more accurate understanding could be gained from results with significantly lowered statistical uncertainties.

quantity	$A \times E$ fit	$\chi^2/\text{dof}$
$m$	$0.080 \pm 0.010$	1.35
$p_T$	$0.074 \pm 0.010$	1.39
$y$	$0.065 \pm 0.009$	1.54

**Table 6.1:** Constant function fit results for  $A \times E$  values calculated for  $m$ ,  $p_T$ , and  $y$  spectra obtained from the O–O data.

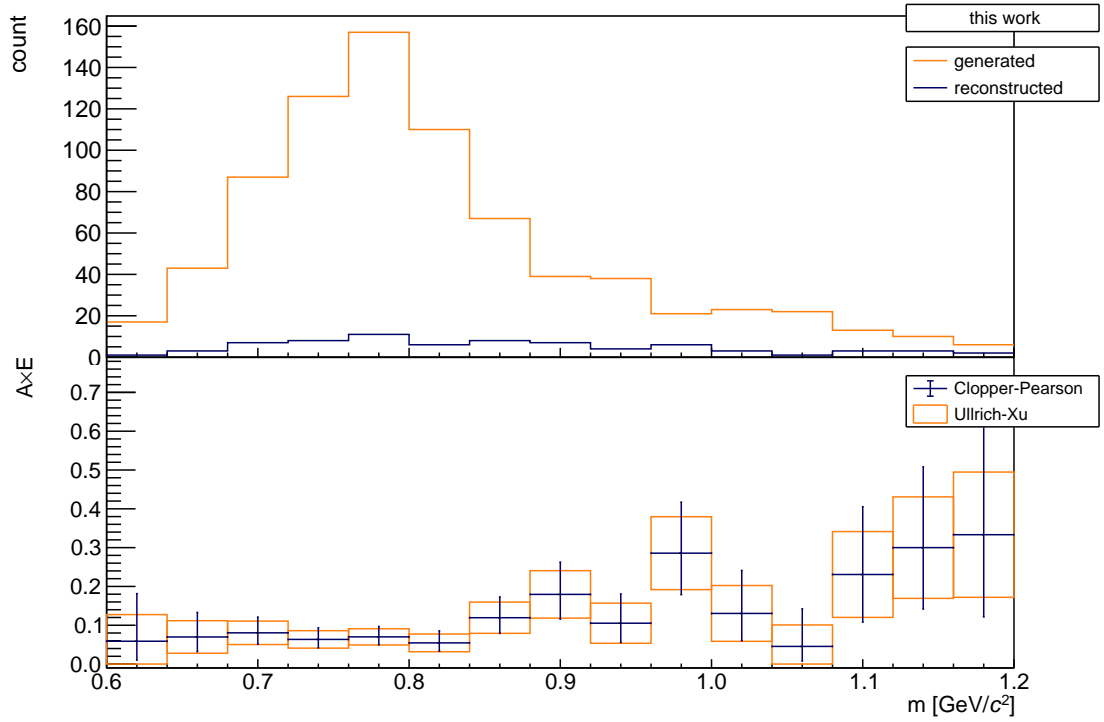


**Figure 6.4:** A×E corrections for  $\rho^0$  invariant mass distribution reconstructed from O–O data.

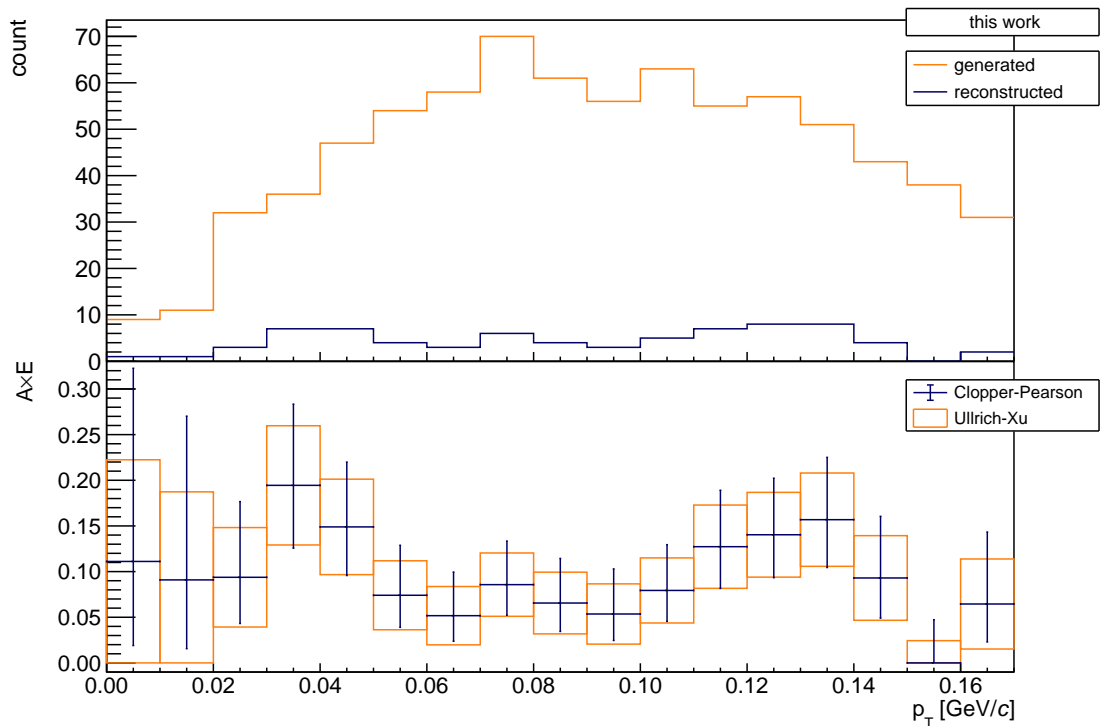


**Figure 6.5:** A×E corrections for  $\rho^0$  transverse momentum distribution reconstructed from O–O data.

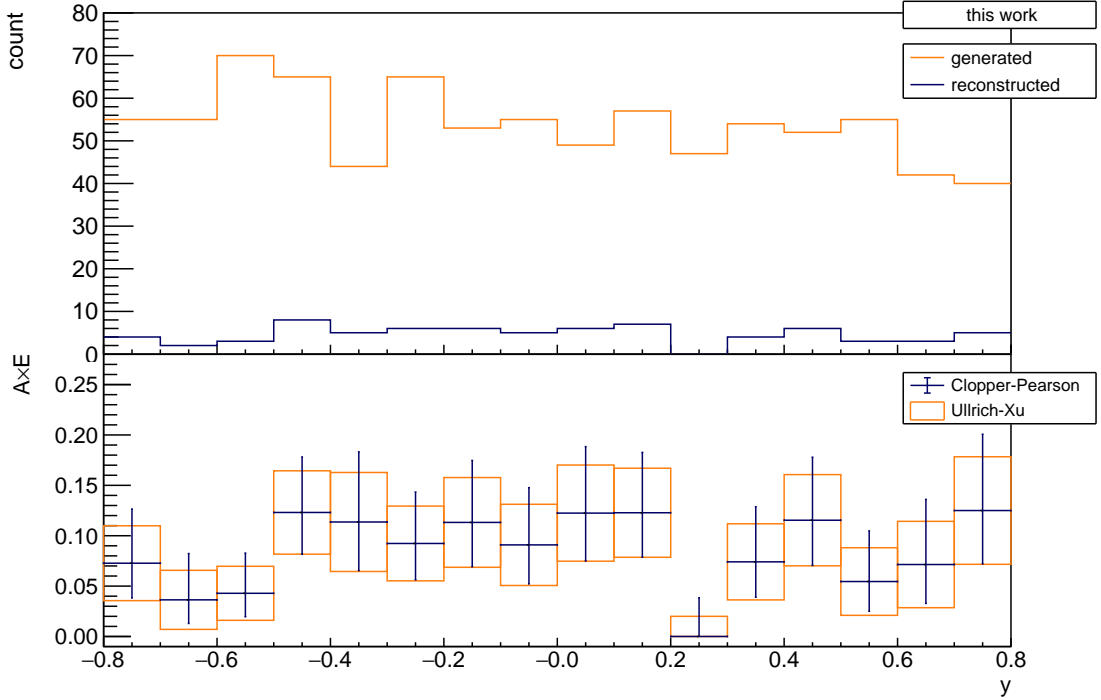


**Figure 6.6:**  $A \times E$  corrections for  $\rho^0$  rapidity distribution reconstructed from O–O data.

## 6.3 Pb–Pb dataset

Essentially the same analysis procedure as described in the previous section was also applied to a dataset of simulated  $\rho^0$  photoproduction in Pb–Pb collisions. Not only is this dataset larger (10000 events), it was also produced using newer software incorporating the most current knowledge of detector responses. Again, the full set of input parameters can be found in Tab. A.1. The settings were largely kept the same as for the oxygen dataset, with the obvious exception being the ion species. The rapidity selection was also shifted to cover only central production, which yields a much greater percentage of the events in the studied interval of  $|y| < 0.8$ . As the treatment of the data is almost exactly the same as with the first dataset, only key differences will be pointed out in this section and unnecessary repetition avoided for the sake of brevity.

### 6.3.1 Generator-level data

Invariant mass, transverse momentum, and rapidity spectra extracted from generator-level data are depicted in Fig. 6.7. The number of events is sufficiently large to observe the second diffraction peak in the  $p_T$  distribution. However, as the performed analysis mimics that of real data, these events will be discarded during the selection of reconstructed events and only the primary peak will be considered. In comparison with the oxygen data, the primary peak is much narrower. This was expected, as the transverse momentum of the produced  $\rho^0$ s is inversely proportional to the radius of the target nucleus participating in the UPC (which is about  $(208/16)^{1/3} \approx 2.35$  times larger for lead).

Transverse momentum, azimuthal angle, and pseudorapidity distributions of the decay products (pions) are plotted in Fig. 6.8. Due to the even lower  $p_T$  of the produced  $\rho^0$ s,  $\Delta\phi$  of the pion tracks is even closer to  $\pi$  (the linear segments in the associated plot are much more defined).

### 6.3.2 Reconstructed data selection

For their consideration for the reconstruction of a  $\rho^0$  meson, each track of the pair was required to have different electric charge and pass the  $|n\sigma_\pi| < 5$  PID requirement.

Selected detector response properties are again presented in Fig. 6.9. The only noticeable difference from Fig. 6.3 is the unsurprising increase in the number of tracks.

The invariant mass and rapidity selections on the reconstructed vector mesons remained the same, i.e.  $0.6 \text{ GeV}/c^2 < m < 1.2 \text{ GeV}/c^2$  and  $|y| < 0.8$ , and the transverse momentum requirement was adjusted to  $p_T < 0.12 \text{ GeV}/c$  to account for the narrower distribution. The low- $m$ , low- $p_T$  tracks were similarly present, as was the case for the oxygen data. In total, 368 out of the 7153 centrally produced  $\rho^0$  mesons passed the selection criteria.

### 6.3.3 $A \times E$ calculation

$A \times E$  values obtained from the reconstructed  $m$ ,  $p_T$ , and  $y$  spectra are plotted alongside them in Figs. 6.10, 6.11, and 6.12. Notable are the much improved statistical uncertainties resulting from the higher number of generated events. From the  $m$  and (to an extent)  $p_T$  results, the  $A \times E$  seems to slightly improve towards higher values, but the statistical uncertainties should be reduced further before reaching any conclusions. Again, a simple constant function fit of the obtained data points was carried out, with its results input into Tab. 6.2. A reduction in the overall value is observed amongst all three studied physical quantities. The larger  $\chi^2/\text{dof}$  for the invariant mass results fit points to the inaccuracy of the presumed constancy of the response.

quantity	$A \times E$ fit	$\chi^2/\text{dof}$
$m$	$0.053 \pm 0.003$	2.27
$p_T$	$0.052 \pm 0.003$	1.09
$y$	$0.049 \pm 0.003$	1.12

**Table 6.2:** Constant function fit results for  $A \times E$  values calculated for  $m$ ,  $p_T$ , and  $y$  spectra obtained from the Pb–Pb data.

## 6.4 Analysis results summary

Although a direct comparison of the results from the previous ALICE Collaboration studies and the analysis performed for this thesis may not be necessarily appropriate, since they differed in their particular procedures and utilised dissimilar software, such an observation may still provide valuable information and will therefore be briefly discussed in this section.

The calculated  $A \times E$  values for the invariant mass distribution extracted from both examined datasets are overall lower compared with those from the presented Pb–Pb photoproduction measurement (Fig. 5.2) and, particularly the result from the lead dataset,

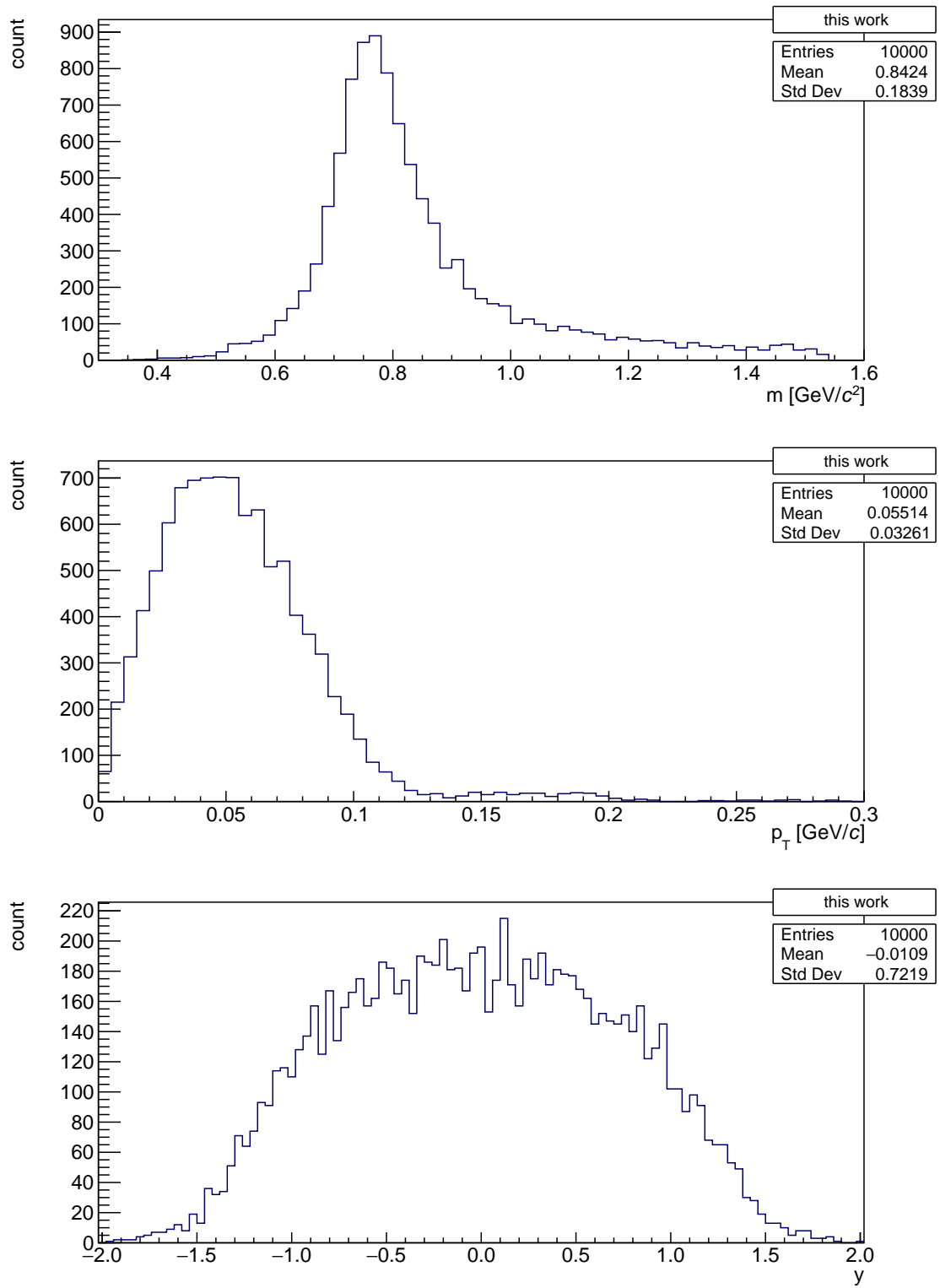


**Figure 6.7:** Generator-level invariant mass, transverse momentum, and rapidity distributions of generated  $\rho^0$  mesons from Pb–Pb events.



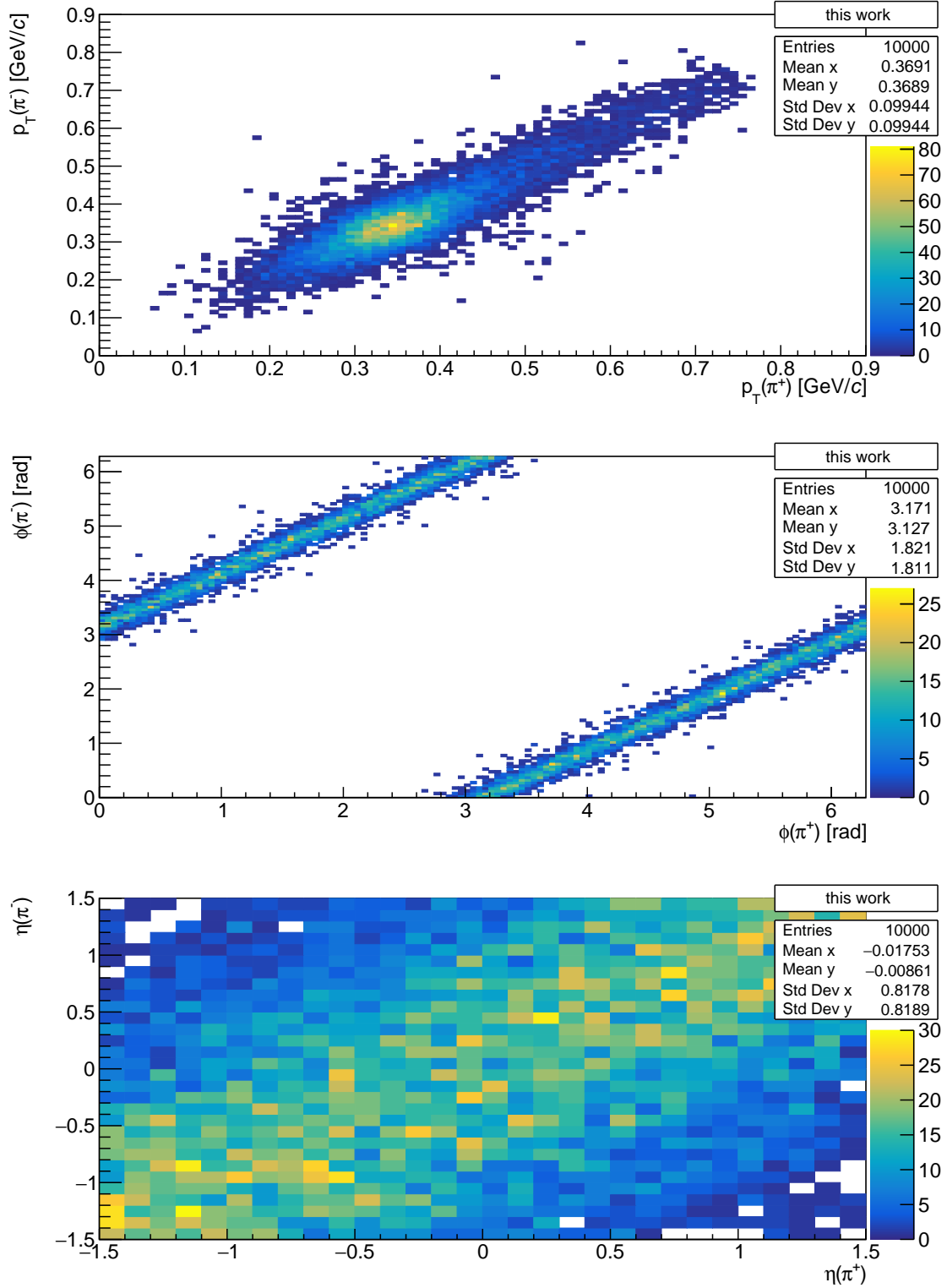


**Figure 6.8:** Transverse momentum, azimuthal angle, and rapidity distributions of generated pion tracks from Pb-Pb events.

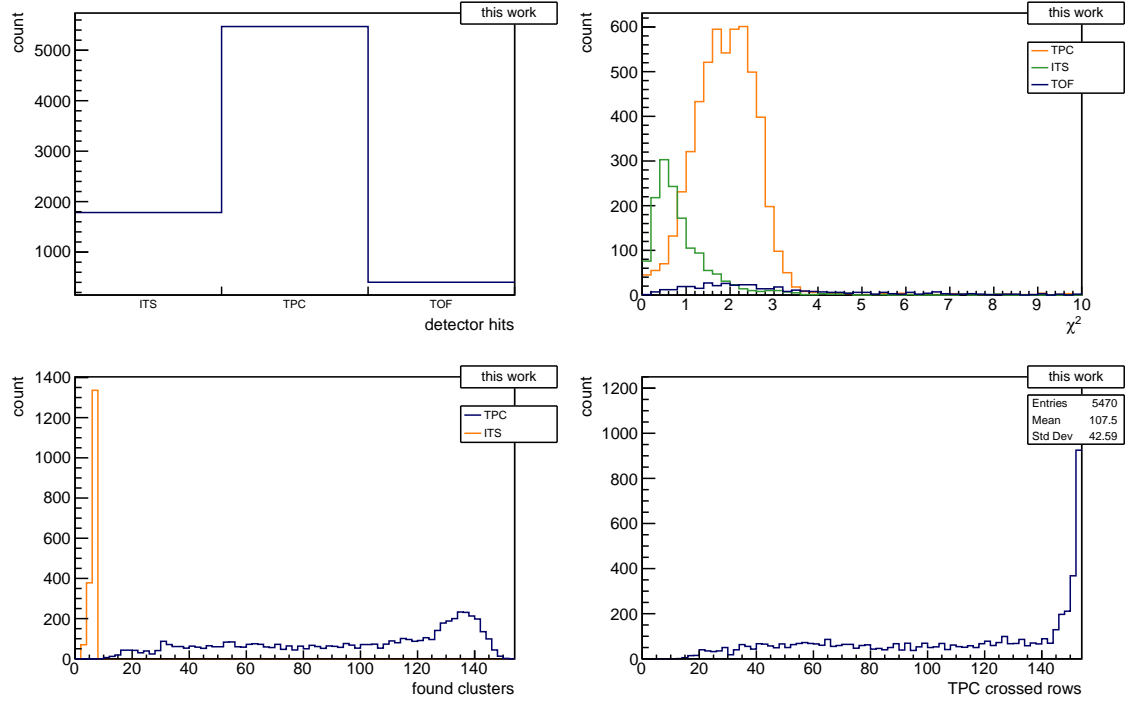


**Figure 6.9:** Select track selection properties of Pb–Pb data reconstructed tracks passing the PID requirement. Shown are the total number of detector hits, the track  $\chi^2$  in the individual detectors, the number of found clusters within the ITS and TPC detectors, and the number of crossed TPC rows.

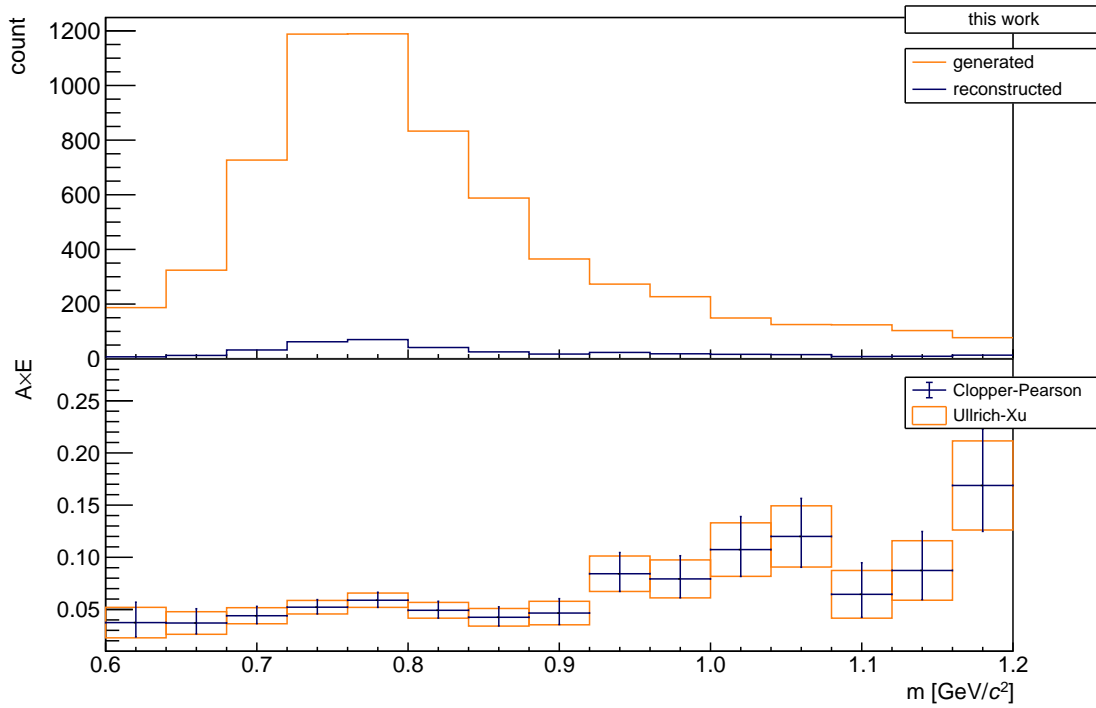


**Figure 6.10:**  $A \times E$  corrections for  $\rho^0$  invariant mass distribution reconstructed from Pb–Pb data.

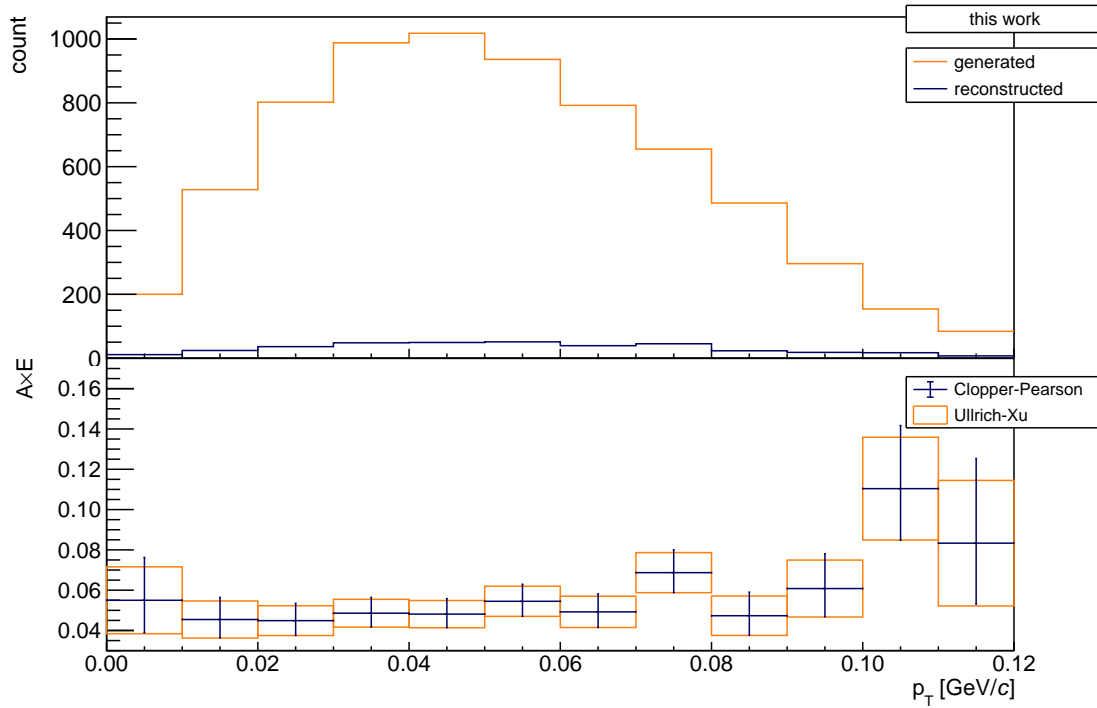


**Figure 6.11:**  $A \times E$  corrections for  $\rho^0$  transverse momentum distribution reconstructed from Pb-Pb data.

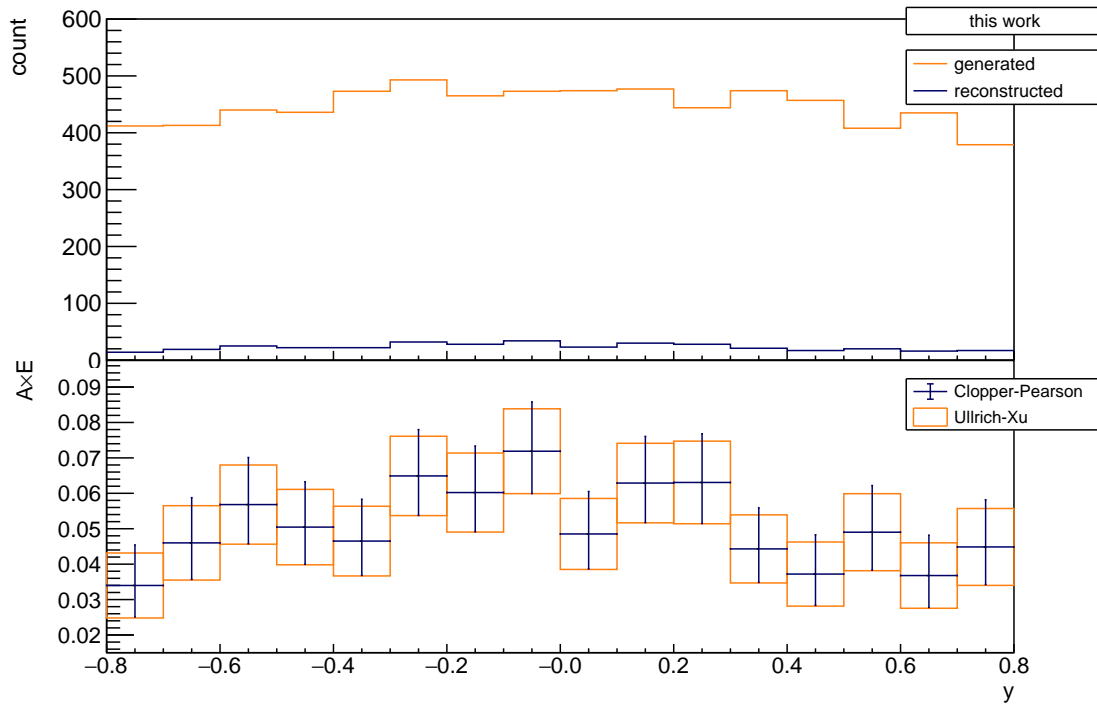


**Figure 6.12:**  $A \times E$  corrections for  $\rho^0$  rapidity distribution reconstructed from Pb-Pb data.

closer to the results from the Xe–Xe study (Fig. 5.6). This is contrary to expectations, which suspected an improvement of the obtained values, and is presumably caused by certain software issues. Specifically, this may include problems with the matching of ITS and TPC tracks, and ambiguities in the assignment of tracks to individual collisions within the continuous readout paradigm. These phenomena are not yet well understood and require further examination.

While the difference in the relative size of statistical uncertainties between the two sets of results complicates this comparison, there is an apparent discrepancy in the results obtained from the two studied datasets (see Tabs. 6.1 and 6.2). As the performed analyses were nearly identical, it is improbable for them to have such a profound effect. A possible cause might be the novelty of the lead dataset. Since it was generated more recently, the simulations were based on the latest understanding of detector responses, which was not available previously.

This thesis represents the first attempt to study acceptance times efficiency corrections with the  $O^2$  framework, using the ALICE detector with its newest upgrades and in continuous readout mode. As written above, the resulting values are lower than expected and also differ between both studied datasets. The exact reason for these discrepancies is uncertain and several potential causes require additional inquiry. Further work is needed to achieve better comprehension of the investigated problematic, nevertheless the pre-prepared analysis framework will facilitate subsequent progress.

# Summary

The main objectives of this thesis were familiarisation with the STARlight model and program utilised in the study of ultra-peripheral collisions, review of previous measurements of coherent  $\rho^0$  photoproduction performed by the ALICE Collaboration, and preliminary analysis of the same process in a simulated O–O dataset in preparation for the arrival of real data.

The opening chapters served an introductory purpose. Chapter 1 provided the definitions of variables and physical quantities commonly used in HEP experiments, and presented a simplified picture of the basics of the Standard Model and its division of elementary particles and fundamental forces. Chapter 2 expanded upon quantum chromodynamics, the theory describing the strong interaction, and investigated its practical implications, which constitute a part of the motivations for the study of photoproduction processes.

Ultra-peripheral collisions and photoproduction, the main subject of this work, were covered in Chapter 3. Presented were also the theoretical aspects and descriptions of these processes, alluding to the main motivation behind their examinations and introducing the STARlight model, which is implemented in the identically named software equally important for photoproduction studies.

Chapter 4 explored the instrumentation used in HEP experiments, mainly the Large Hadron Collider, the largest particle accelerator in the world. A brief overview of its technology and operation was provided, with more attention given to the surveyed collision systems. Here, the proposed O–O system was introduced. The ALICE detector was covered in more detail. Particular importance was given to its numerous subdetector systems and their upgrades ahead of the recently commenced LHC Run 3 and the switch to a novel data collection paradigm.

Two previous measurements of coherent photoproduction of the  $\rho^0$  meson in Pb–Pb and Xe–Xe collisions performed by the ALICE Collaboration were summarised in Chapter 5.

Lastly, the analysis of  $\rho^0$  photoproduction performed on two simulated datasets was described in Chapter 6. The datasets were inspected on generator as well as reconstruction level, and the spectra procured following their analysis were used for the calculation of acceptance times efficiency ( $A \times E$ ) correction factors.

With the recent start of Run 3, the LHC and ALICE are to deliver a large amount of data for analysis. Exciting is also the prospect of real data from O–O collisions, which are presently scheduled for 2024. This would present an immense opportunity for expansion of the preliminary analysis and the continuation of the work performed for the preparation of this thesis.

# Appendix A

## STARlight setup parameters

parameter	O setup	Pb setup	note
BEAM_1_Z	8	82	charge of beam 1
BEAM_1_A	16	208	nucleon number of beam 1
BEAM_2_Z	8	82	charge of beam 2
BEAM_2_A	16	208	nucleon number of beam 2
BEAM_1_GAMMA	3864.32	2705.37	Lorentz boost for beam 1
BEAM_2_GAMMA	3864.32	2705.37	Lorentz boost for beam 2
W_MAX	-1	-1	use default for $\gamma\gamma$ CM energy ( $w$ )
W_MIN	-1	-1	use default for $w$
W_N_BINS	50	50	number of bins for $w$
RAP_MAX	10.0	1.5	maximum rapidity of produced particle
RAP_N_BINS	200	200	number of bins for rapidity
CUT_PT	0	0	no restriction on transverse momentum
PT_MIN	1.00	0.01	minimum $p_T$
PT_MAX	3.00	3.00	maximum $p_T$
CUT_ETA	1	1	restriction on pseudorapidity
ETA_MIN	-4.0	-1.5	minimum pseudorapidity
ETA_MAX	1.5	1.5	maximum pseudorapidity
PROD_MODE	3	3	coherent photoproduction
N_EVENTS	2500	10000	number of events
PROD_PID	113	113	selected production channel
RND_SEED	-1	5574533	random number generator seed
BREAKUP_MODE	5	5	no requirement on ion breakup
INTERFERENCE	0	0	no interference
IF_STRENGTH	1.00	0.05	strength of interference
INT_PT_MAX	0.24	0.24	maximum $p_T$ for interference
INT_PT_N_BINS	120	120	number of bins for interference $p_T$
XSEC_METHOD	1	1	cross section calculation method

**Table A.1:** Full list of utilised STARlight setup parameters. Note that parameters associated with a disabled setting (e.g. set interference strength with disabled interference) do not take effect during the execution of the program. More detailed descriptions and the remainder of unused settings can be found in Ref. [12].

# Bibliography

- [1] James E. Dodd and Ben Gripaios. *The Ideas of Particle Physics*. 4th. Cambridge University Press, Sept. 2020. ISBN: 978-1-108-61627-0, 978-1-108-72740-2. DOI: 10.1017/9781108616270.
- [2] Matic Lubej. *Standard Model LaTeX images*. Accessed on 03/02/2023. May 2022. URL: <https://github.com/mlubej/standard-model>.
- [3] R. L. Workman et al. “Review of Particle Physics”. *PTEP* 2022 (2022), p. 083C01. DOI: 10.1093/ptep/ptac097.
- [4] A. R. Erwin et al. “Evidence for a  $\pi\pi$  Resonance in the  $I = 1, J = 1$  State”. *Phys. Rev. Lett.* 6 (1961), pp. 628–630. DOI: 10.1103/PhysRevLett.6.628.
- [5] Spencer R. Klein and Heikki Mäntysaari. “Imaging the nucleus with high-energy photons”. *Nature Rev. Phys.* 1.11 (2019), pp. 662–674. DOI: 10.1038/s42254-019-0107-6. arXiv: 1910.10858 [hep-ex].
- [6] F. D. Aaron et al. “Combined Measurement and QCD Analysis of the Inclusive  $e^\pm p$  Scattering Cross Sections at HERA”. *JHEP* 01 (2010), p. 109. DOI: 10.1007/JHEP01(2010)109. arXiv: 0911.0884 [hep-ex].
- [7] Nestor Armesto. “Nuclear shadowing”. *J. Phys. G* 32 (2006), R367–R394. DOI: 10.1088/0954-3899/32/11/R01. arXiv: hep-ph/0604108.
- [8] A. Adeluyi and G. Fai. “Mass dependence of nuclear shadowing at small Bjorken- $x$  from diffractive scattering”. *Phys. Rev. C* 74 (2006), p. 054904. DOI: 10.1103/PhysRevC.74.054904. arXiv: hep-ph/0610214.
- [9] A. J. Baltz. “The Physics of Ultraperipheral Collisions at the LHC”. *Phys. Rept.* 458 (2008), pp. 1–171. DOI: 10.1016/j.physrep.2007.12.001. arXiv: 0706.3356 [nucl-ex].
- [10] J. G. Contreras and J. D. Tapia Takaki. “Ultra-peripheral heavy-ion collisions at the LHC”. *International Journal of Modern Physics A* 30.08 (2015), p. 1542012. DOI: 10.1142/S0217751X15420129.
- [11] Spencer R. Klein and Joakim Nystrand. “Exclusive vector meson production in relativistic heavy ion collisions”. *Physical Review C* 60.1 (1999). DOI: 10.1103/physrevc.60.014903. arXiv: hep-ph/9902259.
- [12] Spencer R. Klein et al. “STARlight: A Monte Carlo simulation program for ultraperipheral collisions of relativistic ions”. *Comput. Phys. Commun.* 212 (2017), pp. 258–268. DOI: 10.1016/j.cpc.2016.10.016. arXiv: 1607.03838 [hep-ph].
- [13] CERN. *Our History*. Accessed on 08/02/2023. URL: <https://www.home.cern/about/who-we-are/our-history>.

- [14] Ewa Lopienska. “The CERN accelerator complex, layout in 2022. Complexe des accélérateurs du CERN en janvier 2022” (2022). General Photo. URL: <https://cds.cern.ch/record/2800984>.
- [15] Lyndon R Evans and Philip Bryant. “LHC Machine”. *JINST* 3 (2008), S08001. DOI: 10.1088/1748-0221/3/08/S08001. URL: <https://cds.cern.ch/record/1129806>.
- [16] Brian Petersen and Filip Moortgart. *Physics expectations and wishes for Run 3*. Accessed on 24/02/2023. Jan. 2023. URL: <https://indico.cern.ch/event/1224987/contributions/5153335/>.
- [17] CERN. *LHC long term schedule*. Accessed on 10/02/2023. URL: <https://lhc-commissioning.web.cern.ch/schedule/LHC-long-term.htm>.
- [18] O. Aberle et al. *High-Luminosity Large Hadron Collider (HL-LHC): Technical design report*. CERN Yellow Reports: Monographs. Geneva: CERN, 2020. DOI: 10.23731/CYRM-2020-0010. URL: <https://cds.cern.ch/record/2749422>.
- [19] Luciano Musa. *Highlights and perspectives from ALICE*. Accessed on 25/03/2023. July 2021. URL: <https://indico.cern.ch/event/879856/contributions/4238667/>.
- [20] CERN. *First lead-ion collisions in the LHC at record energy*. Accessed on 10/02/2023. URL: <https://home.cern/news/news/experiments/first-lead-ion-collisions-lhc-record-energy>.
- [21] C. A. Salgado et al. “Proton–Nucleus Collisions at the LHC: Scientific Opportunities and Requirements”. *J. Phys. G* 39 (2012), p. 015010. DOI: 10.1088/0954-3899/39/1/015010. arXiv: 1105.3919 [hep-ph].
- [22] M. Schaumann et al. “First Xenon–Xenon Collisions in the LHC”. *Proc. 9th International Particle Accelerator Conference (IPAC’18)*. International Particle Accelerator Conference 9. JACoW Publishing, June 2018, pp. 180–183. ISBN: 978-3-95450-184-7. DOI: 10.18429/JACoW-IPAC2018-MOPMF039.
- [23] R. Bruce. *Ions – outlook for 2023 and beyond*. Accessed on 24/02/2023. Jan. 2023. URL: <https://indico.cern.ch/event/1224987/contributions/5153630/>.
- [24] ALICE Collaboration. *ALICE physics projections for a short oxygen-beam run at the LHC*. Tech. rep. ALICE-PUBLIC-2021-004. <https://cds.cern.ch/record/2765973>. 2021.
- [25] R. Bruce et al. “Studies for an LHC Pilot Run with Oxygen Beams”. *12th International Particle Accelerator Conference*. Aug. 2021. DOI: 10.18429/JACoW-IPAC2021-MOPAB005.
- [26] K. Aamodt et al. “The ALICE experiment at the CERN LHC”. *JINST* 3 (2008), S08002. DOI: 10.1088/1748-0221/3/08/S08002.
- [27] ALICE Collaboration. “ALICE upgrades during the LHC Long Shutdown 2”. CERN-EP-2023-009 (Feb. 2023). arXiv: 2302.01238.
- [28] G. Herrera Corral. “Diffractive Physics with ALICE at the LHC: the control of quantum collisions”. *Journal of Physics: Conference Series* 624.1 (June 2015), p. 012008. DOI: 10.1088/1742-6596/624/1/012008.
- [29] Solangel Rojas. “The Forward Diffractive Detector for ALICE”. *PoS LHCP2020* (2021), p. 221. DOI: 10.22323/1.382.0221.



- [30] Maciej Slupecki. “Fast Interaction Trigger for ALICE upgrade”. *Nuclear Instruments and Methods in Physics Research Section A: Accelerators, Spectrometers, Detectors and Associated Equipment* 1039 (2022), p. 167021. DOI: 10.1016/j.nima.2022.167021.
- [31] ALICE Collaboration. “ALICE luminosity determination for Pb–Pb collisions at  $\sqrt{s_{\text{NN}}} = 5.02$  TeV” (Apr. 2022). arXiv: 2204.10148 [nucl-ex].
- [32] P Buncic, M Krzewicki, and P Vande Vyvre. *Technical Design Report for the Upgrade of the Online–Offline Computing System*. Tech. rep. Apr. 2015. URL: <https://cds.cern.ch/record/2011297>.
- [33] Chiara Zampolli. “ALICE data processing for Run 3 and Run 4 at the LHC”. *PoS ICHEP2020* (2021), p. 929. DOI: 10.22323/1.390.0929. arXiv: 2012.04391 [physics.ins-det].
- [34] ALICE Collaboration. “Coherent photoproduction of  $\rho^0$  vector mesons in ultra-peripheral Pb–Pb collisions at  $\sqrt{s_{\text{NN}}} = 5.02$  TeV”. *JHEP* 06 (2020), p. 35. DOI: 10.1007/JHEP06(2020)035. arXiv: 2002.10897 [nucl-ex].
- [35] ALICE Collaboration. “First measurement of coherent  $\rho^0$  photoproduction in ultra-peripheral Xe–Xe collisions at  $\sqrt{s_{\text{NN}}} = 5.44$  TeV”. *Phys. Lett. B* 820 (2021), p. 136481. DOI: 10.1016/j.physletb.2021.136481. arXiv: 2101.02581 [nucl-ex].
- [36] David Horák. “Measurement of  $\rho^0$  photoproduction at high energies with the ALICE detector”. Dissertation. Czech Technical University in Prague, 2022. URL: <https://dspace.cvut.cz/handle/10467/106768>.
- [37] ALICE Collaboration. *O<sup>2</sup> Project: o2::constants::physics Namespace Reference*. Accessed on 10/07/2023. URL: [https://aliceo2group.github.io/docs/d7/df9/namespaco2\\_1\\_1constants\\_1\\_1physics.html#a3d71e0c604f1baec02d3f1ac76b07fdf](https://aliceo2group.github.io/docs/d7/df9/namespaco2_1_1constants_1_1physics.html#a3d71e0c604f1baec02d3f1ac76b07fdf).
- [38] *ROOT: TEfficiency Class Reference*. Accessed on 11/07/2023. URL: <https://root.cern.ch/doc/master/classTEfficiency.html#ae80c3189bac22b7ad15f57a1476ef75b>.
- [39] T. Ullrich and Z. Xu. “Treatment of Errors in Efficiency Calculations” (2012). arXiv: physics/0701199 [physics.data-an].